

Spatiotemporal Graph Learning with Direct Volumetric Information Passing and Feature Enhancement

Yuan Mi
Renmin University of China
Beijing, China
miyuan@ruc.edu.cn

Qi Wang
Renmin University of China
Beijing, China
qi_wang@ruc.edu.cn

Xueqin Hu
Wuhan University of Technology
Wuhan, China
hxq@whut.edu.cn

Yike Guo
Hong Kong University Of Science and
Technology
Hong Kong, China
yikeguo@ust.hk

Ji-Rong Wen
Renmin University of China
Beijing, China
jrwen@ruc.edu.cn

Yang Liu
University of Chinese Academy of
Sciences
Beijing, China
liuyang22@ucas.ac.cn

Hao Sun*
Renmin University of China
Beijing, China
haosun@ruc.edu.cn

Abstract

Data-driven learning of physical systems has kindled significant attention, where many neural models have been developed. In particular, mesh-based graph neural networks (GNNs) have demonstrated significant potential in modeling spatiotemporal dynamics across arbitrary geometric domains. However, the existing node-edge message-passing and aggregation mechanism in GNNs limits the representation learning ability. In this paper, we proposed a dual-module framework, Cell-embedded and Feature-enhanced Graph Neural Network (aka, CeFeGNN), for learning spatiotemporal dynamics. Specifically, we embed learnable cell attributions to the common node-edge message passing process, which better captures the spatial dependency of regional features. Such a strategy essentially upgrades the local aggregation scheme from first order (e.g., from edge to node) to a higher order (e.g., from volume and edge to node), which takes advantage of volumetric information in message passing. Meanwhile, a novel feature-enhanced block is designed to further improve the model's performance and alleviate the over-smoothness problem. Extensive experiments on various PDE systems and one real-world dataset demonstrate that CeFeGNN achieves superior performance compared with other baselines.

CCS Concepts

• **Computing methodologies** → **Modeling and simulation; Artificial intelligence**; • **Applied computing** → **Physics**.

*Corresponding authors.

Permission to make digital or hard copies of all or part of this work for personal or classroom use is granted without fee provided that copies are not made or distributed for profit or commercial advantage and that copies bear this notice and the full citation on the first page. Copyrights for components of this work owned by others than the author(s) must be honored. Abstracting with credit is permitted. To copy otherwise, or republish, to post on servers or to redistribute to lists, requires prior specific permission and/or a fee. Request permissions from permissions@acm.org.
KDD '26, Jeju, ON, South Korea

© 2026 Copyright held by the owner/author(s). Publication rights licensed to ACM.
ACM ISBN 978-1-4503-XXXX-X/2018/06
<https://doi.org/XXXXXXXX.XXXXXXX>

Keywords

Graph learning, spatiotemporal prediction, higher-order dynamics

ACM Reference Format:

Yuan Mi, Qi Wang, Xueqin Hu, Yike Guo, Ji-Rong Wen, Yang Liu, and Hao Sun. 2026. Spatiotemporal Graph Learning with Direct Volumetric Information Passing and Feature Enhancement. In *Proceedings of Proceedings of the 32nd ACM SIGKDD Conference on Knowledge Discovery and Data Mining V.1 (KDD '26)*. ACM, New York, NY, USA, 19 pages. <https://doi.org/XXXXXXXX.XXXXXXX>

1 Introduction

Neural surrogate models are often essential for analyzing and modeling complex spatiotemporal dynamics processes across various scientific and engineering fields. For example, weather prediction [23, 63, 64], ocean current motion prediction [78], nonlinear engineering structure earthquake response prediction [76], material mechanical properties simulation [71], etc. Traditionally, classical numerical methods (e.g., Finite Difference Method (FDM) [22, 53], Finite Volume Method (FVM) [16], and Finite Element Method (FEM) [30]) are utilized to solve these PDEs, requiring substantial analytical or computational efforts. Although this problem has been simplified via discretizing the space, the issue of trade-off between cost and precision intensifies when dealing with varying domain geometries (e.g., different initial or boundary conditions or various input parameters), especially in real-world scenarios. In the last few decades, Deep Learning (DL) [1, 35, 57, 66, 67] models have made great progress in approximating high-dimensional PDEs benefiting from existing rich labeled or unlabeled datasets. However, there are certain drawbacks in this simple approach of learning the nonlinear mapping between inputs and outputs from data. For example, their performance is severely limited by the training datasets, the neural network lacks interpretability and generalizes poorly.

Embedding domain-specific expertise (e.g., Physics-informed Neural Networks (PINNs) [58]) has shown the potential to tackle these problems [18, 28, 37, 45]. However, the core part of PINNs, *Automatic Differentiation (AD)* approach, has two major drawbacks:

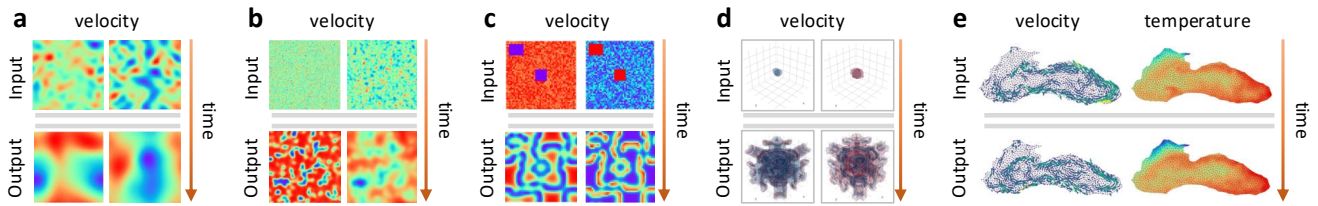


Figure 1: Examples of datasets, including classic governing equations and complex real-world dataset. a, the 2D Burgers equation. b, the 2D Fitzhugh-Nagumo equation. c, the 2D Gray-Scott equation. d, the 3D Gray-Scott equation. e, the 2D Black-Sea dataset.

(1) it is necessary to formulate explicit governing equations into the loss function, and (2) the parameters in high-dimensional feature spaces cannot be efficiently optimized when facing highly complex networks like graph networks. As shown in Figure 1e, there are no any predefined equations available to represent the evolution patterns of sea surface temperature at varying depths. Neural Operators, such as DeepONet [49] and Latent DeepONet [34], have emerged as another paradigm to learn these complex non-linear behaviors. The most well-known models, Fourier Neural Operator (FNO) [42] and its variants [4, 41, 68, 72], utilize neural networks to learn parameters in the Fourier space for fast and effective turbulence simulation. Likewise, they inevitably have the same shortcoming as those traditional methods: over-reliance on data and biased towards the grid domain.

The other representative models, Transformer models [69, 74] and GNNs [19, 29, 48, 50], have demonstrated significant influence in predicting spatiotemporal dynamics across arbitrary geometric domains. In particular, mesh-based graph neural networks (GNNs) [8, 20, 21, 56] learn vastly different dynamics of various physical systems, ranging from structural mechanics and cloth to fluid simulations. However, the existing node-edge message passing mechanism in GNNs overestimates the primary role of “message” passing function on the neighbor “edges”, limiting the model’s representation learning ability. In general, this strategy leads to highly homogeneous node features after multiple rounds of message passing, making the features ineffective at representing distinct characteristics, namely, the over-smoothness problem.

To further address the above issues, we proposed an end-to-end graph-based framework, Cell-embedded and Feature-enhanced Graph Neural Network (CeFeGNN), to model spatiotemporal dynamics across various domains with improved performance. Specifically, after detecting discontinuities in space, we embed learnable cell attributions into the existing node-edge message passing process, which better captures the spatial dependency of regional features and legitimately learns higher-order information from connected nodes of any cell. This cell-embedded (CE) method allows us to rapidly identify non-local relationships that traditional message-passing mechanisms often fail to capture directly. Essentially, such a strategy upgrades the local aggregation scheme from the first order (e.g., from edge to node) to a higher order (e.g., from volume and edge to node), which takes advantage of volumetric information in message passing. Meanwhile, a novel feature-enhanced (FE) block is designed to further improve the model’s performance and relieve the over-smoothness problem via treating the latent features as basis functions and further processing these features on this concept. In details, it regards the node feature \mathbf{h}_i as basis and builds a

higher-order feature via an outer-product operation, e.g., $\mathbf{h}_i \otimes \mathbf{h}_i$. This process creates abundant high-order nonlinear terms to enrich the feature map when it is applied iteratively. We then use a mask operation to randomly sample these terms, filtering the appropriate information by a learnable weight tensor to enhance the model’s representation capacity. Figure 2 shows an outline of our proposed model. Extensive experimental results on many PDE-centric systems and real-world datasets show that CeFeGNN significantly enhance spatiotemporal learning in various scenarios, particularly with limited training datasets. The dual-module structure based on the synergy between the cell-embedded module and the FE module enables our model to effectively extract and process interaction features that are better serving for for complex dynamics learning. The key contributions are summarized as follows:

- We introduce a two-level cell-embedded message-passing mechanism to better capture the spatial dependency on complex domains, which is not only easy to follow but also lightweight yet effective.
- We propose a unique feature-enhanced (FE) block to learn the high-order features and capture dynamic interactions, which conforms to empirical intuition.
- Extensive experiments demonstrate that our approach stands out for its lower error and robust generalizability in the spatiotemporal dynamic field.

2 Related Works

Spatiotemporal dynamics research, as one of the important frontier research areas, is integral to fields ranging from traditional fluid dynamics to economics and finance. In this part, we firstly give a brief introduction to spatiotemporal PDEs. Then, the relevant progress in spatiotemporal dynamics research is described from the perspectives of classical and neural solvers.

2.1 Problem statement

Without loss of generality, the time-dependent systems generally describe the evolution of a continuous field over certain time intervals, which can be cast into the following form: $\partial \mathbf{u} / \partial t = \mathcal{F}(\theta, t, \mathbf{x}, \mathbf{u}, \nabla \mathbf{u}, \nabla^2 \mathbf{u}, \dots)$, where $\mathcal{F}(\cdot)$ denotes an unknown linear or nonlinear function comprised of the spatiotemporal variable $\mathbf{u}(\mathbf{x}, t) \in \mathbb{R}^d$, its corresponding partial derivatives (e.g., $\nabla \mathbf{u}$, $\nabla^2 \mathbf{u}$), and some related parameters θ . Here, $\mathbf{x} \in \mathbb{R}^m$ denotes the m -dimensional spatial coordinate, $t \in \mathbb{R}^1$ the time, ∇ the Nabla operator, ∇^2 the Laplacian operator. Our task is **to predict the states of all subsequent moments after a random initial condition.**

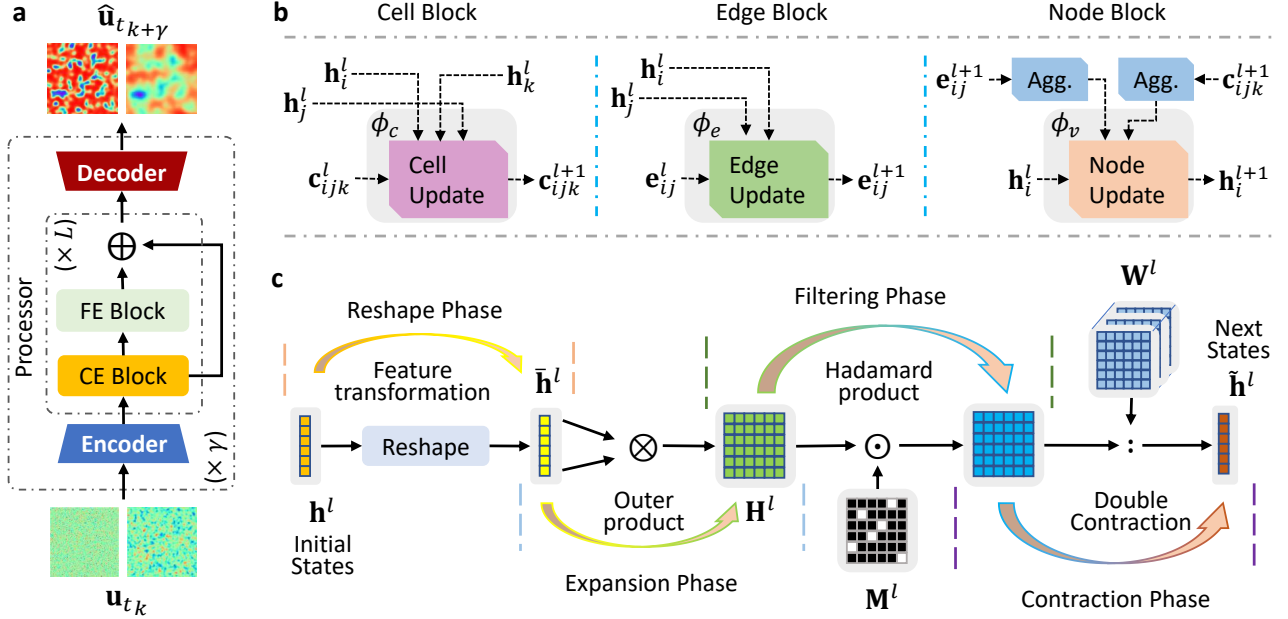


Figure 2: Network architecture of CeFeGNN. a, an encoder encodes the physical variables to latent features, multiple message passing blocks process these latent features iteratively, and a decoder maps back to the physical states. b, three components in the CE block. c, the process of FE block. The definition of relative symbols refers to Section 3.

2.2 Classical solvers

To solve time-dependent PDEs, a common way is the method of lines (MOL). By discretizing in all but one dimension, it allows solutions to be computed via methods and software developed for the numerical integration of ordinary differential equations (ODEs) and differential-algebraic equations (DAEs). Meanwhile, the multigrid method [73] is another algorithm for solving PDEs via a hierarchy of discretizations. Other classical numerical methods (e.g., Finite Difference Method (FDM) [22, 53], Finite Volume Method (FVM)[16], and Finite Element Method (FEM)[12]) have also been utilized for practical applications [30, 60].

2.3 Neural solvers

2.3.1 PINN Methods. Two main approaches, Physics-informed Neural networks (PINNs) [28, 37, 58] and Physics-informed Neural Operators (PINOs) [27, 36, 44], were developed to learn fluid and solid mechanisms. With formulating the explicit governing equation as the loss function, PINNs and PINOs constrain the latent feature spaces to a certain range, effectively learning from small data or even without any labeled data. Such novel methods immediately attract the attention of many researchers and has been utilized in a wide range of applications governed by differential equations, such as heat transfer problems [11], power systems [52], medical science [62], and control of dynamical systems [3].

2.3.2 Neural Operators. Common neural operators [34, 49] combine various basis transforms (e.g., Fourier, multipole kernel, wavelet [24]) with neural networks to accelerate PDE solvers in diverse applications. For example, Fourier Neural Operator (FNO) and its variants [4, 45, 68, 72] learn parameters in the Fourier domain for turbulence simulation. Especially, Geo-FNO [41] maps the irregular

domain into a uniform mesh with a specific geometric Fourier transform to fit irregular domains. However, they all follow the assumptions of periodicity and time-invariance property, making them fail in complex boundaries. Their excellent performance “illusion” in turbulent flow is primarily due to their turbulence solver closely related to the Fourier transform.

2.3.3 Transformer Methods. As another paradigm, Transformer [69] and its “x-former” family [32, 74] have also been utilized to solve complex PDEs. Given the attention mechanism along with a higher complexity, many researchers are trying to alleviate this issue through various means. For example, linear attention mechanism [27, 43] is a well-known method to address this limitation. Although the above methods alleviate the need for specific domain expertise, they all share the same limitations: instability in long-range prediction and weak generalization ability.

2.3.4 Graph Methods. Abundant works about Graph Neural Networks (GNNs) [18, 19, 29, 48] and geometric learning [10, 25, 26, 29] attempt to utilize customized substructures to generalize message passing to more complex domains. For example, graph kernel methods [2, 40] try to learn the implicit or explicit embedding in Reproducing Kernel Hilbert Spaces (RKHS) for identifying differential equations. [6] considers solving the problem of predicting fluid flow using GNNs. [46] introduces the interpolation strategy and the finite element method into GNNs. [17] constructs the multi-scale message-passing dependency. [7] perform message passing on simplicial complexes (SCs). Most notably, MPNNs [20, 21, 31, 55] are utilized to tackle these issues, which learn latent representations on graphs via message passing mechanism. Especially, MeshGraphNets [56] and MP-PDE solver [8] are two representative examples. While powerful and expressive, we still find that there are some

problems with these methods: (1) *their expression ability is still not strong enough*, (2) *their prediction error is still somewhat high*, and (3) *they still rely on a large amount of data*. Hence, we designed our model to address these three problems.

3 Methodology

In this section, we illustrate how our method effectively learn the solution of spatiotemporal PDEs under various parameters (e.g., the initial or boundary conditions, constant or variable coefficients) for a given physical system. All the source code and data would be posted after peer review.

3.1 Network architecture

To enhance the performance of long-range prediction, we adapt the conventional “Encoder-Processor-Decoder” framework in [8, 56] as the backbone of our method, which is primarily designed to effectively learn the complex spatiotemporal dependencies on graphs. As shown in Figure 2, our proposed method mainly consists of the Feature-Enhanced (FE) block and the Cell-Embedded (CE) block. These two key components update features in a sequential process to achieve the cascaded enhancement effect that: (1) Updating node-edge-cell features with the CE block; (2) Enriching higher-order node features with the FE block; (3) Iteratively repeating the above two steps until the specified number of processor layers is reached. The synergy of these two sequentially placed blocks in turn improves the model’s representation learning capacity and generalization ability. The source code and data are provided at <https://www.github.com> (posted after the peer-review process).

3.1.1 Feature-enhanced block. For the sake of brevity and clarity, FE block, shown in Figure 2, is designed to enhance the latent features from the upstream block and further alleviate the over-smoothness issue commonly seen in GNNs due to excessive aggregation. Please see the ablation results on FE’s efficacy in Table 4. More details are provided in Appendix Section C.3.

Outer Product as Basis Expansion. The outer product operation \otimes on the reshaped feature map $\bar{\mathbf{h}}_i \in \mathbb{R}^{D \times 1}$ expands the original latent feature space into a higher-order tensor space. This expansion introduces second-order terms (e.g., $\alpha\beta$ for $\{\alpha, \beta\} \in \bar{\mathbf{h}}_i$), which can capture interactions between individual components of the original feature $\mathbf{h}_i \in \mathbb{R}^D$. Mathematically, the second-order tensor reads $\bar{\mathbf{h}}_i \otimes \bar{\mathbf{h}}_i$. This operation creates a richer feature map with cross-term interactions that may not be explicitly encoded in the original latent space.

Lemma 3.1 (Nonlinear Representation). *The second-order terms $\alpha\beta$ can model nonlinear dependencies between features. This is particularly useful for capturing complex interactions that linear transformations (e.g., via simple dot products) might overlook.*

Definition 3.2. The FE block expands the latent feature $\bar{\mathbf{h}}_i \in \mathbb{R}^{D \times 1}$ of node i into a higher-order feature map $\mathbf{H}_i \in \mathbb{R}^{D \times D}$ using an outer product: $\mathbf{H}_i = \bar{\mathbf{h}}_i \otimes \bar{\mathbf{h}}_i$.

Regularization via Masking. Masking introduces sparsity in \mathbf{H}_i , reducing overfitting. If \mathbf{M}_{jk} is selected, $\mathbf{M}_{jk} = 1$. Otherwise, $\mathbf{M}_{jk} = 0$. Here j and k index the $\mathbf{M} \in \mathbb{R}^{D \times D}$ components.

Learnable Filtering. The learnable weight tensor $\mathbf{W} \in \mathbb{R}^{D \times D \times D}$ acts as a filter, selecting and emphasizing the most informative terms from upstream tasks.

Definition 3.3. A mask tensor $\mathbf{M} \in \mathbb{R}^{D \times D}$ is applied to randomly sample elements in \mathbf{H}_i , and the resulting masked tensor is processed using a learnable weight tensor $\mathbf{W} \in \mathbb{R}^{D \times D \times D}$ as follows: $\tilde{\mathbf{h}}_i = (\mathbf{M} \odot \mathbf{H}_i) : \mathbf{W}$, where \odot represents element-wise multiplication and $:$ denotes double contraction of tensors. The resulting feature $\tilde{\mathbf{h}}_i \in \mathbb{R}^{1 \times D}$ enriches the representation of $\mathbf{h}_i \in \mathbb{R}^D$.

Corollary 3.4 (Representation Power). *The full feature map \mathbf{H}_i contains D^2 terms for a D -dimensional input feature vector \mathbf{h}_i . After masking, the effective representation space reduces by the sparsity of \mathbf{M} . The learnable filter \mathbf{W} further narrows this down to the most critical terms.*

Considering the GPU memory requirements caused by additional parameters in the FE module, we further provide a feature splitting scheme within latent features to dramatically reduce the number of parameters and computation cost caused by the full FE block (see Figure 3). This strategy divides every feature into multiple sub-features with different window sizes, and then processes each part separately. Finally, these sub-features are combined for next layer learning. Note that we utilize the simplest window method to split the features in this article. Please see the ablation results on the effect of the window size and number of sub-feature on the feature splitting scheme in Table 6.

3.1.2 Cell-embedded block. Generally, traditional message passing (MP) mechanism can be regarded as a refinement on a discrete space, analogous to an interpolation operation, which implies that edges are essentially interpolated from nodes. A MP mechanism introducing the cell has potential to further enhance the refinement of the discrete space (namely, secondary refinement), thereby reducing the magnitude of discretization errors spatially and paving the way for its application in complex domains.

Definition 3.5 (Cell in Graphs). For a graph $G = (V, E)$, where V is the set of nodes v and $E \subseteq V \times V$ is the set of edges, a cell in G is a subset of nodes $C \subseteq V$, such that the nodes in C form a complete subgraph (clique) or satisfy predefined structural relationships. In particular, a k -cell C_k in a graph G contains $k + 1$ nodes. Consider $\forall (i, j, k, \dots) \in C_k$ and $(\mathbf{e}_{ij}, \mathbf{e}_{jk}, \dots) \in E$, various structures could be formulated, such as node ($k = 0$), edge ($k = 1$), triangle ($k = 2$), tetrahedron ($k = 3$), and so on. Figure 4 depicts the cell in graphs.

Corollary 3.6 (Expressive Power). *Given a graph G including many k -cell ($k = 0, 1, 2, \dots$), there exists a cell-based scheme that is more expressive than Weisfeiler-Lehman (WL) tests in distinguishing non-isomorphic graphs (see the proof in Supplementary C.2).*

Therefore, we proposed a two-level cell-embedded mechanism to process the message on graphs. A detailed framework with cell-embedded features is designed as the following description.

Remark 3.7. Our method is geometry-agnostic, where the cell (e.g., triangle, quad, hexagon, tetrahedron) is not a limiting prior but rather input-adaptive guidance. The message-passing scheme learns geometric relations without shape-specific assumptions, ensuring universal applicability to diverse geometries as demonstrated in experiments spanning 2D/3D regular/irregular meshes.

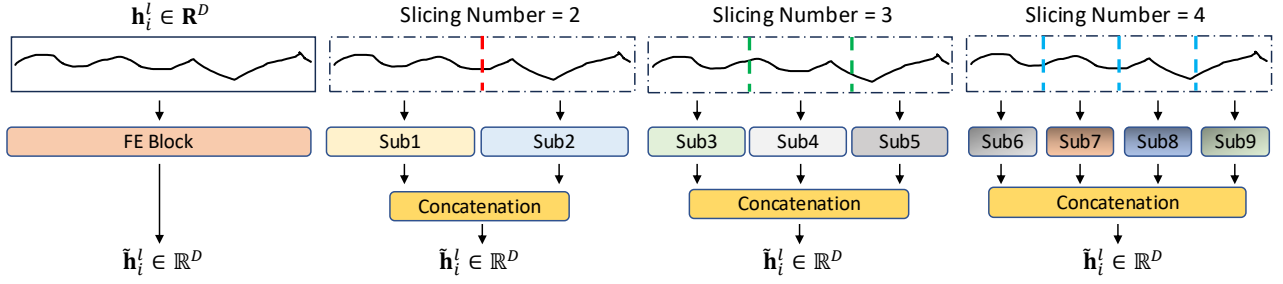


Figure 3: A scheme for reducing the number of parameters in FE block. Its quantitative experiment of the impact of window size and number of sub-features on CeFeGNN is shown in Table 6.

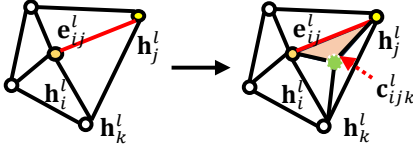


Figure 4: Cell in graphs. Green point is the centroid of cell.

3.1.3 Main Architecture.

Encoder. The encoder block maps the low-dimensional variables to corresponding high-dimensional latent features via differential functions (e.g., MLPs). The initial node feature \mathbf{h}_i^0 includes the node feature, one-hot feature of node type, and their position information. The initial edge feature \mathbf{e}_{ij}^0 contains the relative position vector, the distance of neighbor nodes, and etc. The initial cell feature \mathbf{c}_{ijk}^0 involves the centroid position of cell, the area of cell, and the relative position vector from three nodes to the corresponding centroid position. The corresponding forms are described as:

$$\mathbf{h}_i^0 = \phi_v^{en}(\mathbf{u}_i, \mathbf{x}_i, \kappa_i, \dots), \quad (1a)$$

$$\mathbf{e}_{ij}^0 = \phi_e^{en}((\mathbf{x}_j - \mathbf{x}_i), d_{ij}, \dots), \quad (1b)$$

$$\mathbf{c}_{ijk}^0 = \phi_c^{en}\left(\left(\mathbf{x}_\tau - \mathbf{x}_{\Delta_{ijk}}\right)_{\tau \in \Delta_{ijk}}, \mathbf{x}_{\Delta_{ijk}}, A_{\Delta_{ijk}}, \dots\right), \quad (1c)$$

where the learnable functions $\phi_v^{en}(\cdot)$, $\phi_e^{en}(\cdot)$, and $\phi_c^{en}(\cdot)$ are applied to learn the latent features of node, edge, and cell; $(\mathbf{x}_j - \mathbf{x}_i)$ a relative position vector between the nodes i and j ; d_{ij} the relative physical distance; κ_i the type of node i ; the $\mathbf{x}_{\Delta_{ijk}}$ the centroid position of the cell Δ_{ijk} ; the $A_{\Delta_{ijk}}$ the area of the cell Δ_{ijk} . In addition, (\cdot, \cdot) denotes the concatenation operation.

Processor. The processor iteratively processes the latent features from the upstream encoder via the CE block. We divided the original edge channel \mathbf{e}_{ij}^l into two parts: itself and its adjacent cells. With this simple process, the node can exchange information with itself (nodal info), its immediate neighbor edges (derivative info), and its adjacent cells (integral info). In general, the cell features \mathbf{c}_{ijk}^{l+1} and edge features \mathbf{e}_{ij}^{l+1} firstly learn the effective information from adjacent nodes features, and then are aggregated to formulate the next node states \mathbf{h}_i^{l+1} .

CE block: The two-level procedure is described as:

$$\mathbf{c}_{ijk}^{l+1} = \phi_c^l(\mathbf{h}_i^l, \mathbf{h}_j^l, \mathbf{h}_k^l, \mathbf{c}_{ijk}^l), \quad (2a)$$

$$\mathbf{e}_{ij}^{l+1} = \phi_e^l(\mathbf{h}_i^l, \mathbf{h}_j^l, \mathbf{e}_{ij}^l), \quad (2b)$$

$$\mathbf{h}_i^{l+1} = \phi_v^l\left(\underbrace{\mathbf{h}_i^l}_{\text{nodal info}}, \underbrace{\sum_{j \in \mathcal{N}_i} \mathbf{e}_{ij}^{l+1}}_{\text{derivative info}}, \underbrace{\sum_{jk \in \mathcal{N}_i} \mathbf{c}_{ijk}^{l+1}}_{\text{integral info}}\right), \quad (2c)$$

where $j \in \mathcal{N}_i$ represents every neighbor edge \mathbf{e}_{ij} at node i ; $jk \in \mathcal{N}_i$ every neighbor cell Δ_{ijk} at node i . ϕ_c^l , ϕ_e^l , and ϕ_v^l are the differential functions of cell, edge, and node at the layer l . Note that we have reformulated the message passing mechanism, where edge and cell features, without interaction, are used to simultaneously update the node features. See the test results of computational cost and scalability in Table 5.

FE block: We apply the FE block on the above node features \mathbf{h}_i^{l+1} to obtain the output node features of the processor that:

$$\tilde{\mathbf{h}}_i^{l+1} = \phi_v^{fe}(\mathbf{h}_i^{l+1}), \quad (3)$$

where ϕ_v^{fe} is the block mentioned in the Section 3.1.1. A detailed diagram is shown in Figure 2c.

Decoder. The decoder maps latent features back to physical variables on graphs. With a skip connection, we acquire new states $\mathbf{u}_{t_{k+1}}$ by incremental learning, described as:

$$\hat{\mathbf{u}}_{i,t_{k+1}} = \phi_v^{de}\left(\tilde{\mathbf{h}}_i^L\right) + \mathbf{u}_{i,t_k}, \quad (4)$$

where $\phi_v^{de}(\cdot)$ is the differentiable function (e.g., MLPs) and L the total number of layers.

4 Experiments

4.1 Datasets and Baselines

To evaluate the performance of CeFeGNN, we experiment on the classic physical problems and more challenging real-world scenarios, including Burgers equation, Gray-Scott Reaction-Diffusion (GS RD) equation, FitzHugh-Nagumo (FN) equation, and Black-Sea (BS) dataset. The first three datasets are generated by various governing equations on the grid domain and the final one on irregular meshes. Here, the initial input fields of three synthetic datasets are generated on Gaussian distribution with various random seeds and the node connectivity is obtained by the Delaunay algorithm. See Appendix Table S2 for a detailed description of these datasets.

All PDE datasets in our paper are benchmarks and publicly available from [8, 46, 59] and the real-world dataset is collected by the CMEMS. More details about dataset generation and source refer to Appendix Section D.1. Moreover, an extension of CeFeGNN on traffic prediction task is provided in Appendix section D.3.5.

We compare our model with the most popular graph-based neural network, such as MeshGraphNet (MGN) [56], Graph Attention Network (GAT) [70], Graph Attention Network Variant (GATv2) [9], the state-of-the-art models, message passing neural PDE solver (MP-PDE) [8], Fourier Neural Operator (FNO) [42], Factorized FNO (FFNO) [68], Geometry-informed FNO (Geo-FNO) [39, 41], Transolver [74]. As shown in Appendix Table S3, a comparative analysis of these baselines is discussed. Additional detailed information about these baselines refers to Appendix Section D.2.

4.2 Experimental setup

In our experiments, we mainly focus on predicting much longer time steps with lower error and attempt to achieve better generalization ability of various initial conditions (ICs) and boundary conditions (BCs). For fairness, we set the feature dimension to 128 and utilize the one-step training strategy (i.e., one-step forward, one-step backward) for all tasks. All experiments are run on one NVIDIA A100 GPU. The Adaptive Moment Estimation (Adam) optimizer [33] and the ReduceLROnPlateau learning scheduler [54] with a decay rate of 0.8 are utilized for the model training. All models are trained by injecting random Gaussian noise of varying standard deviation to the input to improve stability during rollout and correct small errors. Meanwhile, Root Mean Square Error (RMSE) loss function is utilized to optimize parameters θ in networks. Given the ground-truth values $Y \in \mathbb{R}^{N \times d}$ and the predictions $\hat{Y} \in \mathbb{R}^{N \times d}$ at time t , the loss function is defined as: $RMSE(Y, \hat{Y}) = \sqrt{\frac{1}{Nd} \sum_{i=1}^N \sum_{j=1}^d (y_{ij} - \hat{y}_{ij})^2}$, where $y_{ij} \in Y$ and $\hat{y}_{ij} \in \hat{Y}$. More details about the experimental setup are described in Appendix Section D.3.

4.3 Results

We consider four different types of study cases: (1) the generalization test, (2) the cell feature’s efficacy, (3) the feature-enhanced effect, and (4) an ablation study. All our experiments revolve around the following question: *Can our model generalize well and achieve lower error with limited data?*

4.3.1 Generalization test. In this part, we varied the initial input field, randomly sampled from a Gaussian distribution with various means and standard deviations, in order to test the generalization ability of all models. According to the analysis results in Figures 5 and 6, we found that CeFeGNN generalizes to different ICs robustly on all benchmarks. It is evident that the performances of CeFeGNN and all baselines in the multi-step long-term prediction vary significantly. However, the experiment results of FNO show that it performs relatively poorly on all datasets except for the Burgers equation. This is a common observation [51] for FNO on other benchmarks, especially with limited training data (e.g., a few to dozens of trajectories considered in this work, rather than thousands used in the original FNO paper). Under such a case, FNO struggles with over-fitting issue and fails to generalize over generic ICs for long-range prediction, especially in the 3D case. The full

Table 1: Results of different methods. “–” represents that the model is unable or unsuitable to learn the dynamics directly. “↓” represents that the smaller the value of the quantitative metric, the better the model performance. The bold values and underlined values represent the optimal and sub-optimal results on various datasets. The abbreviation “Pro.” represents promotion calculated from the above two. We describe the time interval with the form “(1.0 s)”.

Model	RMSE ↓				
	2D Burgers (0.001 s)	2D FN (0.002 s)	2D GS (0.25 s)	3D GS (0.25 s)	2D BS (1 day)
GAT	0.11754	0.02589	0.07227	0.06396	0.62954
GATv2	0.11944	0.03827	0.07301	0.04519	0.64796
MGN	<u>0.01174</u>	<u>0.02108</u>	<u>0.02917</u>	<u>0.01925</u>	0.61475
MP-PDE	0.01784	0.02848	0.03860	0.06528	<u>0.60761</u>
FNO	0.05754	0.12643	0.11331	0.17163	–
FFNO	0.03341	0.11921	0.03628	0.03594	–
Geo-FNO	0.59363	20.514	0.18669	NaN	1.28931
Transolver	0.17422	0.13724	0.18594	0.15204	0.81991
Ours	0.00664	0.00364	0.00248	0.00138	0.55599
Pro. (%) ↑	43.4	82.9	91.4	92.8	8.4

snapshots of 3D GS dataset are displayed in Appendix Figure S3. The variant of FNO, FFNO, outperforms FNO across all datasets. Unexpectedly, Geo-FNO, which incorporates the IPHI technique, achieves the worst performance. Similarly, Transolver underperforms in all cases. Given the experimental results of above baselines, we can infer that these methods exhibit poor generalization ability on small datasets, falling short compared to graph-based methods.

All results listed in Table 1 demonstrate that all graph-based models have great generalization ability. GATv2, the advanced variant of GAT, underperforms GAT on Burgers, FN, 2D GS RD, and BS datasets, but outperforms GAT on 3D GS RD equation, yet both methods fall short of MGN. Surprisingly, the performance of MP-PDE is mediocre. Although MP-PDE is trained by the multi-step prediction strategy during the training stage, its results are only slightly better than MGN on the BS dataset. In contrast, our method performs robustly with much smaller errors in the multi-step prediction problem on all datasets.

4.3.2 The efficacy of cell features. We also have test the efficacy of cell features on the performance of graph-based baselines across all benchmarks with various methods and report the results with RMSE metrics in the Table 2 below to support our claim of introducing cells. We can intuitively see that the introduction of cell feature has a positive effect on all graph-based models, showing that our lightweight and decoupling alternative two-level cell-embedded message passing mechanism could better capture the spatial dependency on complex graphs. The consistent performance improvement (e.g., the promotions of “MGN + Cell” and “MP-PDE + Cell”) not only exhibits strong practicability of cell features but also reflects a right breakthrough to improve the traditional “black-box” neural network via the prior knowledge (e.g., geometric concept) embedded mechanism.

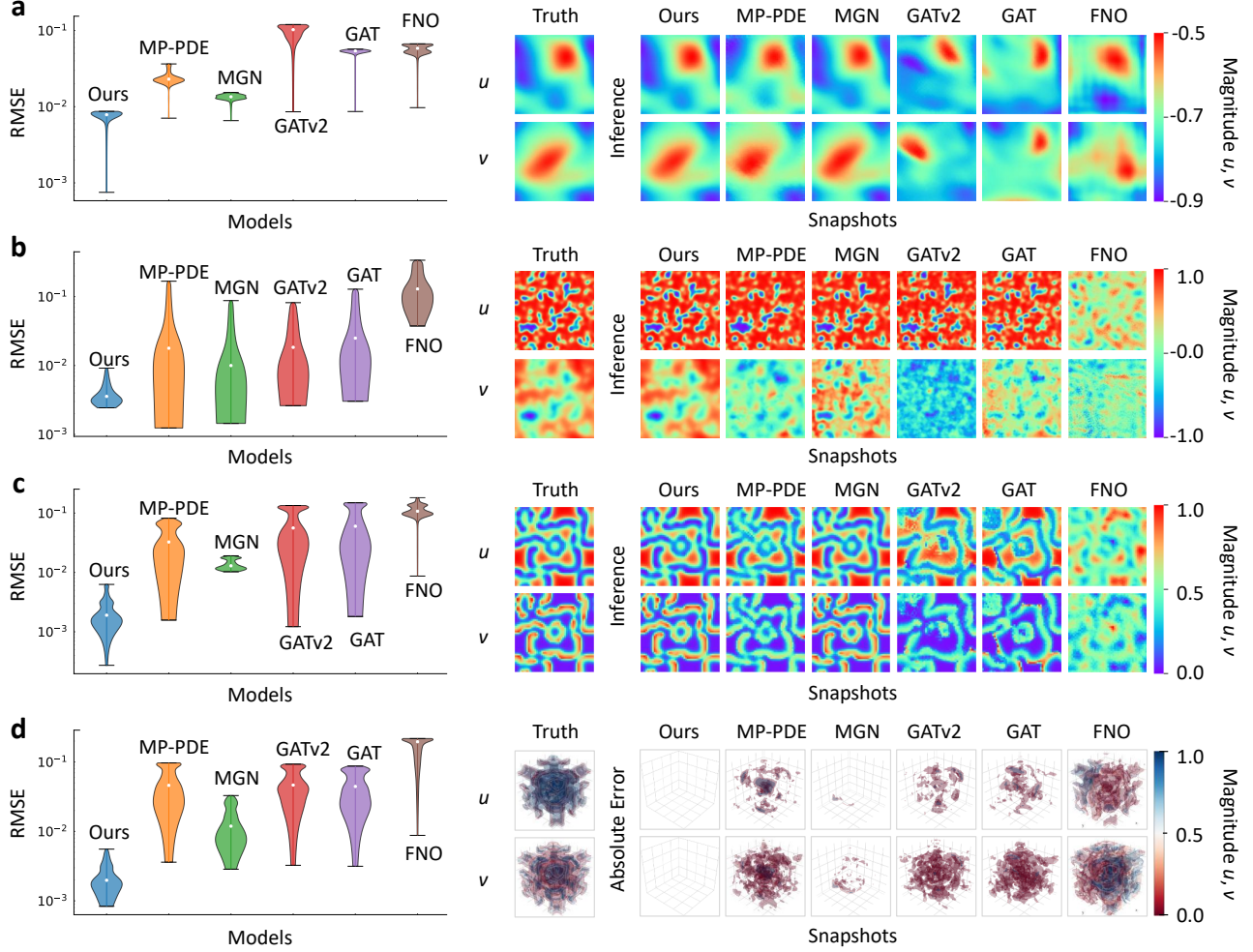


Figure 5: The test results of all models on various datasets. a-d, the error distribution and the slices of generalization test on four grid-based datasets. The full snapshots of 3D GS dataset are displayed in Appendix Figure S3. The results of 2D BS dataset are displayed in Figure 6. Error propagation curves refer to Appendix Section D.3.8.

4.3.3 Feature-enhanced effect. We investigate the effectiveness of the FE block on all graph-based network over all datasets. The results are reported in Table 3, showing that the feature-enhanced block somewhat changes the performance of these networks. We can directly see that this module has improved the performance of all baselines on real-world datasets. Specifically, it achieves the best and worst promotions in the cases of “MGN + FE” on the 3D GS RD equation and “GATv2 + FE” on the 2D Burgers equation. Intriguingly, after embedding the FE block in the processor block, the attention-based graph networks (e.g., GAT and GATv2) perform worse on the governing equation and better on the real-world dataset (even though the promotion is not large). This negative impact of the FE block on attention-based methods is essentially due to a logical conflict of design motivation. Consider two adjacent nodes \mathbf{h}_1 and \mathbf{h}_2 near a node \mathbf{h}_0 , the attention mechanism assigns normalized weights w_1 and w_2 (e.g., $w_1 + w_2 = 1$) and aggregates features by the summation operation like $w_1\mathbf{h}_1 + w_2\mathbf{h}_2$. However, the FE block would disrupt this global normalization rule

Table 2: Efficacy of cell features on the performance of graph-based baselines across all benchmarks.

Model	RMSE ↓				
	2D Burgers (0.001 s)	2D FN (0.002 s)	2D GS (0.25 s)	3D GS (0.25 s)	2D BS (1 day)
MGN	0.01174	0.02108	0.02917	0.01925	0.61475
+ Cell	0.00826	0.00791	0.00832	0.00694	0.58019
Pro. (%) ↑	29.6	62.4	71.4	63.9	5.6
MP-PDE	0.01784	0.02848	0.03860	0.06528	0.60761
+ Cell	0.00951	0.01193	0.00947	0.00992	0.59313
Pro. (%) ↑	46.7	58.1	75.4	84.8	2.38

in the attention mechanism and reduces the expression capability of attention-based methods.

4.3.4 Ablation study. In this part, we perform an ablation study on all datasets to assess the contributions of the FE and CE blocks in

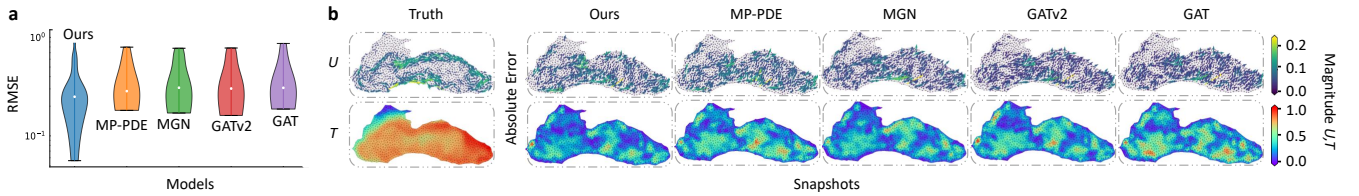


Figure 6: The test results of all models on BS Dataset. a, the error distribution. b, the prediction at the 10th time step. Error propagation curves refer to Appendix Section D.3.8. The full snapshots on BS dataset refer to Appendix Figure S4.

Table 3: Efficacy of the FE block on the performance of graph-based baselines across all benchmarks.

Model	RMSE ↓				
	2D Burgers (0.001 s)	2D FN (0.002 s)	2D GS (0.25 s)	3D GS (0.25 s)	2D BS (1 day)
GAT	0.11754	0.02589	0.07227	0.06396	0.62954
+ FE	0.15132	0.02717	0.08527	0.07058	0.61984
Pro. (%) ↑	-28.7	-4.9	-17.9	-10.3	1.5
GATv2	0.11944	0.03827	0.07301	0.04519	0.64796
+ FE	0.18496	0.04117	0.09365	0.06432	0.63363
Pro. (%) ↑	-54.8	-7.5	-28.2	-43.2	2.2
MGN	0.01174	0.02108	0.02917	0.01925	0.61475
+ FE	0.00817	0.01241	0.01583	0.00721	0.60593
Pro. (%) ↑	30.4	41.1	45.7	62.5	1.4
MP-PDE	0.01784	0.02848	0.03860	0.06528	0.60761
+ FE	0.01445	0.01957	0.02621	0.03655	0.60372
Pro. (%) ↑	18.9	31.2	32.1	41.5	0.6

Table 4: Quantitative results of ablation study on CeFeGNN. The abbreviation “C” represents the cell.

Model	RMSE ↓				
	2D Burgers (0.001 s)	2D FN (0.002 s)	2D GS (0.25 s)	3D GS (0.25 s)	2D BS (1 day)
w/o C, FE	0.01174	0.02108	0.02917	0.01925	0.61475
w/o C	<u>0.00828</u>	0.00982	0.01035	0.00680	<u>0.58236</u>
w/o FE	0.00877	<u>0.00788</u>	<u>0.00803</u>	<u>0.00679</u>	0.58271
Ours	0.00664	0.00364	0.00248	0.00138	0.55599

CeFeGNN, as shown in Table 4. The results indicate that, without the introduction of the cell, the assembly of the traditional node-edge message passing mechanism and FE block still shows good generalization ability, even with small data. Although we attempt to make the model learn higher-order information in each round, the results demonstrate that the cell-embedded mechanism did not achieve the desired performance, which means that the network architecture of traditional MPNNs still has the over-smoothness problems that need a better solution.

As shown in Table 5, our model with similar parameter ranges achieves the best performance compared with MGN and MP-PDE. We have verified that the improvement of our model performance is due to the innovative use of cell features rather than the introduction of additional parameters. For precision-oriented tasks (e.g.,

Table 5: Quantitative results of computational cost and scalability of CeFeGNN. Note that the dimension of latent feature is set as 128. The abbreviation “Param.” represents the number of parameter. “L” is the total number of processor.

Model	L	Param.	Training (s/epoch)	GPU usage (GB)	2D Burgers ↓ (0.001 s)
MGN	4	514,236	8.64	32.56	0.01174
MGN	12	1,438,086	20.90	74.81	0.01858
MP-PDE	4	528,658	7.86	33.23	0.01784
MP-PDE	12	1,230,533	17.44	76.63	0.10101
w/o FE	4	971,916	14.86	45.85	<u>0.00877</u>
Ours	4	1,482,674	17.31	45.87	0.00664

Table 6: Quantitative results of the impact of window size and number of sub-features of CeFeGNN. Note that the number for window size and sub-feature is described by the form like “(1/128)”. The abbreviation “Param.” represents the number of parameter.

Case	Param.	RMSE ↓			
		2D Burgers (0.001 s)	2D FN (0.002 s)	2D GS (0.25 s)	3D GS (0.25 s)
(1/128)	9,362,572	<u>0.00665</u>	0.00409	0.00251	0.00122
(2/64)	3,071,116	0.00714	<u>0.00370</u>	0.00232	0.00192
(4/32)	1,482,674	0.00664	0.00364	<u>0.00248</u>	<u>0.00138</u>
(8/16)	1,105,036	0.01263	0.02261	0.03481	0.04128
(16/8)	1,006,736	0.11753	0.12900	0.09120	0.18963

modeling PDEs), some trade-off in terms of speed while achieving much higher precision is acceptable. For example, compared to suboptimal models, CeFeGNN achieves a RMSE reduction of $10 \times$ or more (see Table 1) on FN and GS datasets. Even without the FE module (see Table 4), our model still yields a $3 \times$ RMSE reduction.

In addition, as shown in Table 6, excessive feature segmentation can disrupt feature correlations and degrade model performance. Thus, we use the splitting method with a proper window size. We also have performed a data scaling test and report the results (data size vs. prediction error) in the Appendix Table S14. The tests were conducted on the Burgers example using varying trajectories as training data. It can be observed that our model with a smaller amount of data has equal or superior performance compared with that of other methods (MGN and MP-PDE) with larger amounts of data. Additionally, we have investigated the effectiveness of the cell feature on graph-based networks over all benchmarks. The results

in Table 2 show the positive efficacy of cell features. A ablation test about the relative cell position information also demonstrates cell's significance, shown in Appendix Table S15. More importantly, the comparison results between two-level and three-level message passing mechanisms in Appendix Table S17 have verified the the rationality of model design motivation.

5 Conclusion

In this paper, we proposed an end-to-end graph-based framework (namely, CeFeGNN) to learn the complex spatiotemporal dynamics. By utilizing the regional information, CeFeGNN predicts future long-term unobserved states and addresses the over-smoothness problem in GNNs. Firstly, the learnable cell attribution in CE block captures the spatial dependency of regional features, upgrading the local aggregation scheme from the first order to a higher order. Secondly, the FE block enriches the node features, maintaining strong representational power even after multiple rounds of aggregation. The superior performance of our model has been demonstrated by extensive experiments. The theoretical analysis (see Section 3, Appendix Section C) and experimental validation (see Section 4, Appendix Section D) differentiate our approach from existing models. Although CeFeGNN achieves superior performance on extensive experiments, there are several directions for future work, including that (1) pushing our model to learn on a finer mesh with more complex boundary conditions, and (2) further exploring the potential of geometric information to learn higher-order attributions in a more refined way, rather than the rough handling in our article. We attempt to accomplish these goals in our future research work.

References

- [1] Saad Albawi, Tareq Abed Mohammed, and Saad Al-Zawi. 2017. Understanding of a convolutional neural network. In *2017 international conference on engineering and technology (ICET)*. Ieee, 1–6.
- [2] Anima Anandkumar, Kamyar Azizzadenesheli, Kaushik Bhattacharya, Nikola Kovachki, Zongyi Li, Burigede Liu, and Andrew Stuart. 2020. Neural operator: Graph kernel network for partial differential equations. In *ICLR 2020 Workshop on Integration of Deep Neural Models and Differential Equations*.
- [3] Eric Aislan Antonelo, Eduardo Camponogara, Laio Oriel Seman, Jean Panaioti Jordanou, Eduardo Rehbein de Souza, and Jomi Fred Hübner. 2024. Physics-informed neural nets for control of dynamical systems. *Neurocomputing* (2024), 127419.
- [4] Md Ashiqur Rahman, Zachary E Ross, and Kamyar Azizzadenesheli. 2023. U-NO: U-shaped Neural Operators. *IEEE Transactions on Machine Learning Research* (2023).
- [5] Lei Bai, Lina Yao, Can Li, Xianzhi Wang, and Can Wang. 2020. Adaptive graph convolutional recurrent network for traffic forecasting. *Advances in neural information processing systems* 33 (2020), 17804–17815.
- [6] Filipe De Avila Belbute-Peres, Thomas Economon, and Zico Kolter. 2020. Combining differentiable PDE solvers and graph neural networks for fluid flow prediction. In *international conference on machine learning*. PMLR, 2402–2411.
- [7] Cristian Bodnar, Fabrizio Frasca, Yuguang Wang, Nina Otter, Guido F Montufar, Pietro Lio, and Michael Bronstein. 2021. Weisfeiler and lehman go topological: Message passing simplicial networks. In *International Conference on Machine Learning*. PMLR, 1026–1037.
- [8] Johannes Brandstetter, Daniel Worrall, and Max Welling. 2022. Message passing neural PDE solvers. (2022).
- [9] Shaked Brody, Uri Alon, and Eran Yahav. 2022. How attentive are graph attention networks? (2022).
- [10] Michael M Bronstein, Joan Bruna, Yann LeCun, Arthur Szlam, and Pierre Vandergheynst. 2017. Geometric deep learning: going beyond euclidean data. *IEEE Signal Processing Magazine* 34, 4 (2017), 18–42.
- [11] Shengze Cai, Zhicheng Wang, Sifan Wang, Paris Perdikaris, and George Em Karniadakis. 2021. Physics-informed neural networks for heat transfer problems. *Journal of Heat Transfer* 143, 6 (2021), 060801.
- [12] Weiming Cao, Weizhang Huang, and Robert D Russell. 1999. Anr-adaptive finite element method based upon moving mesh PDEs. *Journal of Computational physics* 149, 2 (1999), 221–244.
- [13] Jing Chen, Haocheng Ye, Zhian Ying, Yuntao Sun, and Wenqiang Xu. 2025. Dynamic Trend Fusion Module for Traffic Flow Prediction. *arXiv preprint arXiv:2501.10796* (2025).
- [14] Ben-Ao Dai, Nengchao Lyu, and Yongchao Miao. 2025. FasterSTS: A Faster Spatio-Temporal Synchronous Graph Convolutional Networks for Traffic flow Forecasting. *arXiv preprint arXiv:2501.00756* (2025).
- [15] Ben-Ao Dai, Bao-Lin Ye, and Lingxi Li. 2024. A novel hybrid time-varying graph neural network for traffic flow forecasting. *arXiv preprint arXiv:2401.10155* (2024).
- [16] Robert Eymard, Thierry Gallouët, and Raphaële Herbin. 2000. Finite volume methods. *Handbook of numerical analysis* 7 (2000), 713–1018.
- [17] Meire Fortunato, Tobias Pfaff, Peter Wirnsberger, Alexander Pritzel, and Peter Battaglia. 2022. Multiscale meshgraphnets. *arXiv preprint arXiv:2210.00612* (2022).
- [18] Han Gao, Luning Sun, and Jian-Xun Wang. 2021. PhyGeoNet: Physics-informed geometry-adaptive convolutional neural networks for solving parameterized steady-state PDEs on irregular domain. *J. Comput. Phys.* 428 (2021), 110079.
- [19] Han Gao, Matthew J Zahr, and Jian-Xun Wang. 2022. Physics-informed graph neural Galerkin networks: A unified framework for solving PDE-governed forward and inverse problems. *Computer Methods in Applied Mechanics and Engineering* 390 (2022), 114502.
- [20] Justin Gilmer, Samuel S Schoenholz, Patrick F Riley, Oriol Vinyals, and George E Dahl. 2017. Neural message passing for quantum chemistry. In *International conference on machine learning*. PMLR, 1263–1272.
- [21] Justin Gilmer, Samuel S Schoenholz, Patrick F Riley, Oriol Vinyals, and George E Dahl. 2020. Message passing neural networks. *Machine learning meets quantum physics* (2020), 199–214.
- [22] Sergei K Godunov and I Bohachevsky. 1959. Finite difference method for numerical computation of discontinuous solutions of the equations of fluid dynamics. *Matematicheskij sbornik* 47, 3 (1959), 271–306.
- [23] Aditya Grover, Ashish Kapoor, and Eric Horvitz. 2015. A deep hybrid model for weather forecasting. In *Proceedings of the 21th ACM SIGKDD international conference on knowledge discovery and data mining*. 379–386.
- [24] Gaurav Gupta, Xiongye Xiao, and Paul Bogdan. 2021. Multiwavelet-based operator learning for differential equations. *Advances in neural information processing systems* 34 (2021), 24048–24062.
- [25] Mustafa Hajji, Kyle Istvan, and Ghada Zamzmi. 2020. Cell complex neural networks. *arXiv preprint arXiv:2010.00743* (2020).
- [26] Mustafa Hajji, Ghada Zamzmi, Theodore Papamarkou, Nina Miolane, Aldo Guzmán-Sáenz, Karthikeyan Natesan Ramamurthy, Tolga Birdal, Tamal K Dey, Soham Mukherjee, Shreyas N Samaga, et al. 2022. Topological deep learning: Going beyond graph data. *arXiv preprint arXiv:2206.00606* (2022).
- [27] Zhongkai Hao, Zhengyi Wang, Hang Su, Chengyang Ying, Yinpeng Dong, Songming Liu, Ze Cheng, Jian Song, and Jun Zhu. 2023. Gnot: A general neural operator transformer for operator learning. In *International Conference on Machine Learning*. PMLR, 12556–12569.
- [28] Di He, Shanda Li, Wenlei Shi, Xiaotian Gao, Jia Zhang, Jiang Bian, Liwei Wang, and Tie-Yan Liu. 2023. Learning physics-informed neural networks without stacked back-propagation. In *International Conference on Artificial Intelligence and Statistics*. PMLR, 3034–3047.
- [29] Masanobu Horie and Naoto Mitsume. 2024. Graph Neural PDE Solvers with Conservation and Similarity-Equivariance. *arXiv preprint arXiv:2405.16183* (2024).
- [30] Thomas JR Hughes. 2012. *The finite element method: linear static and dynamic finite element analysis*. Courier Corporation.
- [31] Steeven Janny, Aurélien Beneteau, Madiha Nadri, Julie Digne, Nicolas Thome, and Christian Wolf. 2023. Eagle: Large-scale learning of turbulent fluid dynamics with mesh transformers. *arXiv preprint arXiv:2302.10803* (2023).
- [32] Jiawei Jiang, Chengkai Han, Wayne Xin Zhao, and Jingyuan Wang. 2023. Pdformer: Propagation delay-aware dynamic long-range transformer for traffic flow prediction. In *Proceedings of the AAAI conference on artificial intelligence*, Vol. 37. 4365–4373.
- [33] Diederik P. Kingma and Jimmy Ba. 2015. Adam: A Method for Stochastic Optimization. In *International Conference on Learning Representations*.
- [34] Katianna Kontolati, Somdatta Goswami, George Em Karniadakis, and Michael D Shields. 2024. Learning nonlinear operators in latent spaces for real-time predictions of complex dynamics in physical systems. *Nature Communications* 15, 1 (2024), 5101.
- [35] Jan Koutník, Klaus Greff, Faustino Gomez, and Juergen Schmidhuber. 2014. A clockwork rnn. In *International conference on machine learning*. PMLR, 1863–1871.
- [36] Nikola Kovachki, Zongyi Li, Burigede Liu, Kamyar Azizzadenesheli, Kaushik Bhattacharya, Andrew Stuart, and Anima Anandkumar. 2023. Neural operator: Learning maps between function spaces with applications to pdes. *Journal of Machine Learning Research* 24, 89 (2023), 1–97.
- [37] Aditi Krishnapriyan, Amir Gholami, Shandian Zhe, Robert Kirby, and Michael W Mahoney. 2021. Characterizing possible failure modes in physics-informed neural networks. *Advances in Neural Information Processing Systems* 34 (2021), 26548–26560.

- [38] Mengzhang Li and Zhanxing Zhu. 2021. Spatial-temporal fusion graph neural networks for traffic flow forecasting. In *Proceedings of the AAAI conference on artificial intelligence*, Vol. 35. 4189–4196.
- [39] Zongyi Li, Daniel Zhengyu Huang, Burigede Liu, and Anima Anandkumar. 2023. Fourier neural operator with learned deformations for pdes on general geometries. *Journal of Machine Learning Research* 24, 388 (2023), 1–26.
- [40] Zongyi Li, Nikola Kovachki, Kamyar Azizzadenesheli, Burigede Liu, Andrew Stuart, Kaushik Bhattacharya, and Anima Anandkumar. 2020. Multipole graph neural operator for parametric partial differential equations. *Advances in Neural Information Processing Systems* 33 (2020), 6755–6766.
- [41] Zongyi Li, Nikola Kovachki, Chris Choy, Boyi Li, Jean Kossaifi, Shourya Otta, Mohammad Amin Nabian, Maximilian Stadler, Christian Hundt, Kamyar Azizzadenesheli, et al. 2024. Geometry-informed neural operator for large-scale 3d pdes. *Advances in Neural Information Processing Systems* 36 (2024).
- [42] Z. Li, N. B. Kovachki, K. Azizzadenesheli, B. Liu, K. Bhattacharya, A. Stuart, and A. Anandkumar. 2021. Fourier Neural Operator for Parametric Partial Differential Equations. In *International Conference on Learning Representations*.
- [43] Zijie Li, Kazem Meidani, and Amir Barati Farimani. 2023. Transformer for partial differential equations' operator learning. *IEEE Transactions on Machine Learning Research* (2023).
- [44] Zongyi Li, Hongkai Zheng, Nikola Kovachki, David Jin, Haoxuan Chen, Burigede Liu, Kamyar Azizzadenesheli, and Anima Anandkumar. 2021. Physics-informed neural operator for learning partial differential equations. *ACM/JMS Journal of Data Science* (2021).
- [45] Zongyi Li, Hongkai Zheng, Nikola Kovachki, David Jin, Haoxuan Chen, Burigede Liu, Kamyar Azizzadenesheli, and Anima Anandkumar. 2024. Physics-informed neural operator for learning partial differential equations. *ACM/JMS Journal of Data Science* 1, 3 (2024), 1–27.
- [46] Marten Lienen and Stephan Günnemann. 2022. Learning the dynamics of physical systems from sparse observations with finite element networks. *International Conference on Learning Representations* (2022).
- [47] Hangchen Liu, Zheng Dong, Renhe Jiang, Jiewen Deng, Jinliang Deng, Qunjun Chen, and Xuan Song. 2023. STAEFormer: spatio-temporal adaptive embedding makes vanilla transformer SOTA for traffic forecasting. *arXiv preprint arXiv:2308.10425* (2023).
- [48] Meng Liu, Hongyang Gao, and Shuiwang Ji. 2020. Towards deeper graph neural networks. In *Proceedings of the 26th ACM SIGKDD international conference on knowledge discovery & data mining*. 338–348.
- [49] Lu Lu, Pengzhan Jin, Guofei Pang, Zhongqiang Zhang, and George Em Karniadakis. 2021. Learning nonlinear operators via DeepONet based on the universal approximation theorem of operators. *Nature machine intelligence* 3, 3 (2021), 218–229.
- [50] Kaitlin McCardle. 2023. Shedding light on GNN affinity predictions. *Nature Computational Science* 3, 12 (2023), 1004–1004.
- [51] Yuan Mi, Pu Ren, Hongteng Xu, Hongsheng Liu, Zidong Wang, Yike Guo, Ji-Rong Wen, Hao Sun, and Yang Liu. 2025. Conservation-informed Graph Learning for Spatiotemporal Dynamics Prediction. *Proceedings of the 31th ACM SIGKDD international conference on knowledge discovery and data mining* (2025).
- [52] George S Misyris, Andreas Venzke, and Spyros Chatzivasileiadis. 2020. Physics-informed neural networks for power systems. In *2020 IEEE power & energy society general meeting (PESGM)*. IEEE, 1–5.
- [53] M Necati Özişik, Helcio RB Orlande, Marcelo J Colaço, and Renato M Cotta. 2017. *Finite difference methods in heat transfer*. CRC press.
- [54] Adam Paszke, Sam Gross, Francisco Massa, Adam Lerer, James Bradbury, Gregory Chanan, Trevor Killeen, Zeming Lin, Natalia Gimelshein, Luca Antiga, et al. 2019. Pytorch: An imperative style, high-performance deep learning library. *Advances in neural information processing systems* 32 (2019).
- [55] Roberto Perera and Vinamra Agrawal. 2024. Multiscale graph neural networks with adaptive mesh refinement for accelerating mesh-based simulations. *Computer Methods in Applied Mechanics and Engineering* 429 (2024), 117152.
- [56] T. Pfaff, M. Fortunato, A. Sanchez-Gonzalez, and P. Battaglia. 2021. Learning Mesh-Based Simulation with Graph Networks. In *International Conference on Learning Representations*.
- [57] Allan Pinkus. 1999. Approximation theory of the MLP model in neural networks. *Acta numerica* 8 (1999), 143–195.
- [58] Maziar Raissi, Paris Perdikaris, and George E Karniadakis. 2019. Physics-informed neural networks: A deep learning framework for solving forward and inverse problems involving nonlinear partial differential equations. *Journal of Computational physics* 378 (2019), 686–707.
- [59] Chengping Rao, Pu Ren, Qi Wang, Oral Buyukozturk, Hao Sun, and Yang Liu. 2023. Encoding physics to learn reaction–diffusion processes. *Nature Machine Intelligence* 5, 7 (2023), 765–779.
- [60] Sebastian Reich. 2000. Finite volume methods for multi-symplectic PDEs. *BIT Numerical Mathematics* 40 (2000), 559–582.
- [61] Pu Ren, Chengping Rao, Yang Liu, Jian-Xun Wang, and Hao Sun. 2022. PhyCRNet: Physics-informed convolutional-recurrent network for solving spatiotemporal PDEs. *Computer Methods in Applied Mechanics and Engineering* 389 (2022), 114399.
- [62] Francisco Sahli Costabal, Yibo Yang, Paris Perdikaris, Daniel E Hurtado, and Ellen Kuhl. 2020. Physics-informed neural networks for cardiac activation mapping. *Frontiers in Physics* 8 (2020), 42.
- [63] Sebastian Scher. 2018. Toward data-driven weather and climate forecasting: Approximating a simple general circulation model with deep learning. *Geophysical Research Letters* 45, 22 (2018), 12–616.
- [64] Martin G Schultz, Clara Betancourt, Bing Gong, Felix Kleinert, Michael Langguth, Lukas Hubert Leufen, Amirpasha Mozaffari, and Scarlet Stadler. 2021. Can deep learning beat numerical weather prediction? *Philosophical Transactions of the Royal Society A* 379, 2194 (2021), 20200097.
- [65] Chao Song, Youfang Lin, Shengnan Guo, and Huaiyu Wan. 2020. Spatial-temporal synchronous graph convolutional networks: A new framework for spatial-temporal network data forecasting. In *Proceedings of the AAAI conference on artificial intelligence*, Vol. 34. 914–921.
- [66] Martin Sundermeyer, Ralf Schlüter, and Hermann Ney. 2012. Lstm neural networks for language modeling. In *Interspeech*, Vol. 2012. 194–197.
- [67] Ilya O Tolstikhin, Neil Houlsby, Alexander Kolesnikov, Lucas Beyer, Xiaohua Zhai, Thomas Unterthiner, Jessica Yung, Andreas Steiner, Daniel Keysers, Jakob Uszkoreit, et al. 2021. Mlp-mixer: An all-mlp architecture for vision. *Advances in neural information processing systems* 34 (2021), 24261–24272.
- [68] Alasdair Tran, Alexander Mathews, Lexing Xie, and Cheng Soon Ong. 2021. Factorized fourier neural operators. *International Conference on Learning Representations* (2021).
- [69] Ashish Vaswani, Noam Shazeer, Niki Parmar, Jakob Uszkoreit, Llion Jones, Aidan N Gomez, Łukasz Kaiser, and Illia Polosukhin. 2017. Attention is all you need. *Advances in neural information processing systems* 30 (2017).
- [70] Petar Veličković, Guillem Cucurull, Arantxa Casanova, Adriana Romero, Pietro Lio, Yoshua Bengio, et al. 2017. Graph attention networks. 1050, 20 (2017), 10–48550.
- [71] Kun Wang and WaiChing Sun. 2018. A multiscale multi-permeability poroplasticity model linked by recursive homogenizations and deep learning. *Computer Methods in Applied Mechanics and Engineering* 334 (2018), 337–380.
- [72] Gege Wen, Zongyi Li, Kamyar Azizzadenesheli, Anima Anandkumar, and Sally M Benson. 2022. U-FNO—An enhanced Fourier neural operator-based deep-learning model for multiphase flow. *Advances in Water Resources* 163 (2022), 104180.
- [73] Chao-Yuan Wu, Ross Girshick, Kaiming He, Christoph Feichtenhofer, and Philipp Krahenbuhl. 2020. A multigrid method for efficiently training video models. In *Proceedings of the IEEE/CVF Conference on Computer Vision and Pattern Recognition*. 153–162.
- [74] Haixu Wu, Huakun Luo, Haowen Wang, Jianmin Wang, and Mingsheng Long. 2024. Transolver: A fast transformer solver for pdes on general geometries. *arXiv preprint arXiv:2402.02366* (2024).
- [75] Bing Yu, Haoteng Yin, and Zhanxing Zhu. 2017. Spatio-temporal graph convolutional networks: A deep learning framework for traffic forecasting. *arXiv preprint arXiv:1709.04875* (2017).
- [76] Ruiyang Zhang, Zhao Chen, Su Chen, Jingwei Zheng, Oral Büyükköztürk, and Hao Sun. 2019. Deep long short-term memory networks for nonlinear structural seismic response prediction. *Computers & Structures* 220 (2019), 55–68.
- [77] Jianli Zhao, Zhongbo Liu, Qiuxia Sun, Qing Li, Xiuyan Jia, and Rumeng Zhang. 2022. Attention-based dynamic spatial-temporal graph convolutional networks for traffic speed forecasting. *Expert Systems with Applications* 204 (2022), 117511.
- [78] Gang Zheng, Xiaofeng Li, Rong-Hua Zhang, and Bin Liu. 2020. Purely satellite data-driven deep learning forecast of complicated tropical instability waves. *Science advances* 6, 29 (2020), eaba1482.
- [79] Hao Zhou, Dongchun Ren, Huaxia Xia, Mingyu Fan, Xu Yang, and Hai Huang. 2021. Ast-gnn: An attention-based spatio-temporal graph neural network for interaction-aware pedestrian trajectory prediction. *Neurocomputing* 445 (2021), 298–308.

A Variables notation

In this part, we present a summary of the variable notations used in our paper, as detailed in Table S1.

B Background: OOD test in Spatiotemporal Prediction

In this part, we would like to clarify the generalization tests with different random ICs in spatiotemporal dynamics are OOD. For a nonlinear PDE system, even if the ICs are IID, the spatiotemporal solution can be OOD, because of the following reasons.

Nonlinearity and Emergence of Complex Patterns. Nonlinear PDEs are characterized by their ability to produce highly complex

Table S1: Summary of Notations.

Calculus	Short Name	Role
Derivative of y with respect to x	dy/dx	Unknown Parameter
Partial derivative of y with respect to x	$\partial y/\partial x$	Unknown Parameter
Gradient of y with respect to x	$\nabla_x y$	Unknown Parameter
Tensor containing derivatives of y with respect to \mathbf{X}	$\nabla_{\mathbf{X}} y$	Unknown Parameter
Jacobian matrix $\mathbf{J} \in \mathbb{R}^{m \times n}$ of $f : \mathbb{R}^n \rightarrow \mathbb{R}^m$	$\partial f/\partial x$	Unknown Parameter
The Hessian matrix of f at input point x	$\nabla_x^2 f(x)$ or $\mathbf{H}(f)(x)$	Unknown Parameter
Definite integral over the entire domain of x	$\int f(x)dx$	Unknown Parameter
Definite integral with respect to x over the set S	$\int_S f(x)dx$	Unknown Parameter
Sets and Graphs	Short Name	Role
The set containing 0 and 1	$\{0, 1\}$	Predefined Variable
The set of all integers between 0 and n	$\{0, 1, \dots, n\}$	Predefined Variable
The real interval including a and b	$[a, b]$	Predefined Variable
The real interval excluding a but including b	$(a, b]$	Predefined Variable
A graph with nodes and edges	$G = (E, V)$	Predefined Variable
Latent Variables	Short Name	Role
The node index	i, j, k	Predefined Variable
The latent node features	\mathbf{h}_i	Predefined Variable
The latent edge features	\mathbf{e}_{ij}	Predefined Variable
The latent cell features	\mathbf{c}_{ijk}	Predefined Variable
Variables	Short Name	Role
x-component of velocity	$u(\mathbf{x}, t)$	Input/Predicted Variable
y-component of velocity	$v(\mathbf{x}, t)$	Input/Predicted Variable
vorticity	$w(\mathbf{x}, t)$	Input/Predicted Variable
pressure	$p(\mathbf{x}, t)$	Input/Predicted Variable
temperature under water	$T(\mathbf{x}, t)$	Input/Predicted Variable
Space and Time	Short Name	Role
x-direction of space coordinate	x	Predefined Variable
y-direction of space coordinate	y	Predefined Variable
z-direction of space coordinate	z	Predefined Variable
time coordinate	t	Predefined Variable
time increment	Δt	Predefined Variable
space increment	$\Delta \mathbf{x}$	Predefined Variable
discrete timestamp at k th step	t_k	Predefined Variable

behavior over time. This nonlinearity can amplify small differences in ICs, leading to the emergence of patterns or behaviors that are vastly different from what was initially expected. Even if the ICs are IID, the interactions dictated by the nonlinear terms in the PDE can cause the solution to evolve in a way that is not reflective of the initial distribution. As a result, the system may exhibit behaviors that are not represented in the original distribution, leading to an OOD trajectory dataset. For example, in the Burgers and FN examples, the ICs are generated based on Gaussian distribution with different random seeds (e.g., IID); however, the corresponding solution trajectories remain OOD judging from the histogram plots.

Chaotic Dynamics. Nonlinear PDEs may exhibit chaotic behavior. In these systems, small perturbations in ICs can lead to exponentially different solutions. Over time, this chaotic evolution

can cause the solution to become highly sensitive to ICs (e.g., the 2D FN and 2D/3D GS RD test data examples shown in Figure 1b-d), resulting in a distribution that is very different from the IID distribution of ICs, yielding an OOD solution space.

Long-term Evolution. In many nonlinear PDEs, solutions tend to evolve toward certain stable structures or steady states known as attractors. These attractors can be complex structures in the solution space. Over time, the solution might converge to or oscillate around these attractors, regardless of the IID nature of ICs (e.g., the Burgers, FN and GS RD examples in our paper). The distribution of solutions near these attractors can be very different from the IC IID distribution. Essentially, the system’s long-term behavior is determined more by the attractors rather than by ICs.

Spatiotemporal Correlations. The assumption of IID ICs implies no spatial/temporal correlations initially. However, the evolving dynamics governed by PDEs can introduce correlations over time. These correlations can lead to a solution that has a distribution quite different from the original IID distribution. The emergence of such correlations indicates that the evolved solution is not just a simple extension of ICs, producing datasets with OOD.

Breaking of Statistical Assumptions. As the system evolves, the assumptions that justified the IID nature of ICs may no longer hold. The dynamics of the PDE can induce structures, patterns, or dependencies that were not present in ICs. As a result, the statistical properties of the evolved solution may diverge from those of ICs, leading to an OOD.

Hence, even though the ICs are IID, the resulting solution trajectories are OOD. This might be a little bit different from our understanding of IID/OOD datasets in common practices of NLP, CV, etc. In addition, we have indeed considered OOD ICs in our tests, e.g., the ICs of the 2D/3D GS RD examples are randomly placed square cube concentrations (1 or 2 square/cube blocks) as shown in Figure 1c-d. The resulting solution datasets are obviously OOD. Therefore, all the results of generalizing to different ICs represent OOD tests. Given the same comparison test sets, our model shows better generalization performance over other baselines.

C Proofs

C.1 Supplementary Definitions, Lemmas, Theorems, Corollaries, or Proofs

Lemma C.1 (Feature Diversity). *Introducing cells enhances feature diversity by encoding higher-order relationships among nodes. Specifically, the basic features in traditional MP mechanism are $\{\mathbf{h}_i, \mathbf{h}_j, \mathbf{e}_{ij}, \mathbf{e}_{ji}\}$, and the basic features in cell-based MP mechanism are $\{\mathbf{h}_i, \mathbf{h}_j, \mathbf{h}_k, \mathbf{e}_{ij}, \mathbf{e}_{jk}, \mathbf{e}_{ki}, \mathbf{c}_{ijk}, \mathbf{c}_{kij}, \mathbf{c}_{jki}\}$. The additional node \mathbf{h}_k provides a richer context, enabling the capture of more complex patterns within one round.*

Lemma C.2 (Reduction in Ambiguity). *Traditional MP methods rely solely on pairwise interactions, which can lead to ambiguity in cases of structural symmetry. Cell-based MP mechanism leverages the higher-order structure, reducing ambiguity by providing additional constraints through relationships between three or more nodes.*

Corollary C.3 (Improved Performance). *Cell-based MP mechanism improves prediction capability by enhancing feature distinguishability through introducing higher-order relationships.*

Corollary C.4 (Suitability for Graphs). *In dense or sparse graphs, cell-based methods outperform traditional methods by capturing multi-node interactions within one round, which are critical for preserving the graph's topology.*

Remark C.5 (Explanation of Corollary 3.6 in our main paper). 1-WL test relies on pairwise node comparisons and cannot distinguish graphs that are symmetric under pairwise relationships. By lifting graphs to a cell-embedded pattern and using cell-based MP mechanism, higher-order interactions are encoded, allowing discrimination of graphs that 1-WL test cannot separate. See the detail proof in Subsection C.2.

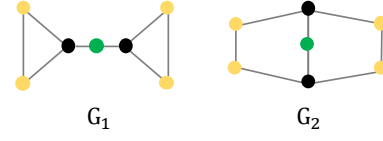


Figure S1: Two undistinguished graphs by 1-WL test. Different colors represent different labels.

C.2 Weisfeiler-Lehman (WL) Tests

Weisfeiler-Lehman (WL) Test is an iterative graph isomorphism algorithm that updates node features by aggregating the features of neighboring nodes. After each iteration, the updated node features are hashed to encode structural information. Despite its effectiveness, WL test cannot distinguish certain non-isomorphic graphs, particularly when higher-order structural information is required. In this part, our goal is to show that cell-based message passing mechanism is more expressive than the 1-WL test for distinguishing non-isomorphic graphs.

Task Definition. A graph $G = (V, E)$ has a set of vertices V and edges E . The 1-WL test iteratively computes node features \mathbf{h}_i^l at iteration l as $\mathbf{h}_i^{l+1} = \text{Hash}(\mathbf{h}_i^l, \{\mathbf{h}_j^l : j \in \mathcal{N}_i\})$, where \mathcal{N}_i is the set of neighbors of i , and \mathbf{h}_i^0 is initialized with the node's feature.

Consider two graphs G_1 and G_2 (see Figure S1), the WL test fails to distinguish G_1 and G_2 because it only aggregates local neighborhood information, and both graphs have identical degree distributions and neighborhood structures for all nodes.

Given that cells (e.g., triangles) can be explicitly considered, we propose a simple cell-based scheme, described as follows.

Initialization. Initializing node features \mathbf{h}_i^0 based on their labels or degrees and initializing higher-order cell features \mathbf{c}_{ijk}^0 by aggregating node features within the triangle.

Message Passing. Updating node and cell features iteratively. For example:

$$\mathbf{h}_i^{l+1} = \text{Hash}(\mathbf{h}_i^l, \{\mathbf{h}_j^l : j \in \mathcal{N}_i\}, \{\mathbf{c}_{ijk}^l : jk \in \mathcal{N}_i\}), \quad (\text{S1a})$$

$$\mathbf{c}_{ijk}^l = \text{Aggregate}(\mathbf{h}_i^l, \mathbf{h}_j^l, \mathbf{h}_k^l), \quad \forall i, j, k \in \Delta_{ijk}. \quad (\text{S1b})$$

Expressiveness. In G_2 , no triangles exist, so all triangle-related features \mathbf{c}_{ijk} will remain zero or absent. (2) In G_1 , there are two triangles. These triangles generate non-zero features that propagate back to nodes during message passing. Thus, the presence of higher-order structures (triangles) allows the cell-based scheme to distinguish G_1 from G_2 . And we proposed the following proposition about the expressiveness of cell-based message-passing scheme.

Proposition C.6. *The cell-based message-passing scheme is more expressive than 1-WL test because it captures higher-order interactions (e.g., triangles) that are invisible to 1-WL. This enhanced capability enables it to distinguish graphs, such as G_1 and G_2 , which cannot be differentiated by 1-WL test.*

C.3 Inspiration of Feature-enhanced (FE) Block

The process of FE block is inspired by interaction models in physics and mathematically hypothesized to capture nonlinear dependencies, enhancing the model’s representation power.

Hypothesis. The FE block’s hypothesis could be framed as: By capturing second-order interactions between latent features and applying selective filtering, the model can better represent complex structures or relationships in the data.

Physical Analogy. In physics, the outer product and second-order terms are often used to model interactions, such as stress tensors in mechanics or pairwise correlations in quantum mechanics. Here, the module could draw an analogy to systems where interactions between individual components (features) are crucial to the overall behavior.

Process Overview. In detail, it regards the node latent feature $\bar{\mathbf{h}}_i \in \mathbb{R}^{D \times 1}$ as basis and builds a higher-order tensor feature $\mathbf{H}_i \in \mathbb{R}^{D \times D}$ via an outer-product operation, e.g., $\bar{\mathbf{h}}_i \otimes \bar{\mathbf{h}}_i$. This process in Algorithm 1 creates abundant second-order nonlinear terms to enrich the feature map. We then use a mask operation with $\mathbf{M} \in \mathbb{R}^{D \times D}$ to randomly sample these terms, filtering the appropriate information by a learnable weight tensor $\mathbf{W} \in \mathbb{R}^{D \times D \times D}$ to enhance the model’s representation capacity.

Algorithm 1: Feature-enhanced block

Input: The current node states $\mathbf{h}^l \in \mathbb{R}^{N \times D}$

Parameter: The weight tensor $\mathbf{W}^l \in \mathbb{R}^{D \times D \times D}$ and the mask matrix $\mathbf{M}^l \in \mathbb{R}^{D \times D}$

Output: The updated node states $\hat{\mathbf{h}}^l \in \mathbb{R}^{N \times D}$

while stop condition is not reached **do**

Step 1: Reshape phase. Reshape the input states \mathbf{h}^l and obtain the $\hat{\mathbf{h}}^l \in \mathbb{R}^{N \times D \times 1}$.

Step 2: Expansion phase. Play an Outer product operation on the $\hat{\mathbf{h}}^l$ to get new states $\mathbf{H}^l \in \mathbb{R}^{N \times D \times D}$.

Step 3: Filtering phase. Filter feature with a Hadamard product operation on the new states \mathbf{H}^l and the mask \mathbf{M}^l to get new states $\hat{\mathbf{H}}^l \in \mathbb{R}^{N \times D \times D}$.

Step 4: Contraction phase. Contract the new states $\hat{\mathbf{H}}^l$ with the weight \mathbf{W}^l by a Double contraction operation to construct the final states $\hat{\mathbf{h}}^l \in \mathbb{R}^{N \times D}$.

end

return The updated states $\hat{\mathbf{h}}^l$.

D Supplementary details of experiments

D.1 Supplementary details of datasets

Viscous Burgers Equation. As a simple non-linear convection–diffusion PDE, Burgers equation generates fluid dynamics on various input parameters. For concreteness, within a given 2D field, there is a velocity $\mathbf{u} = [u, v]^T$ at per 2D grid point. Its general formulation is expressed as following description:

$$\partial \mathbf{u} / \partial t + \mathbf{u} \cdot \nabla \mathbf{u} = \mathbf{D} \nabla^2 \mathbf{u}, \quad (\text{S2})$$

where viscosity $\mathbf{D} = [D_u, D_v]$ is the diffusion coefficient of fluid, $\mathbf{u}(\mathbf{x}, t)$ its velocity, \mathbf{x} the 2D spatial coordinate and t the 1D temporal

coordinate. In this work, we generate the simulation trajectory within $\Omega \in [0, 1]^2$ and $t \in [0, 1](s)$, using a 4th-order Runge–Kutta time integration method [61] under the periodic condition. Here, we define $D_u = 0.01, D_v = 0.01, \Delta t = 0.001(s)$ and $\Delta x = 0.02$.

Fitzhugh-Nagumo Equation. Fitzhugh-Nagumo equation consists of a non-linear diffusion equation with different boundary conditions. We generates the training and testing data $\mathbf{u} = [u, v]^T$ in a given 2D field with periodic boundary conditions:

$$\partial u(\mathbf{x}, t) / \partial t = D_u \nabla^2 u + u - u^3 - v^3 + \alpha, \quad (\text{S3a})$$

$$\partial v(\mathbf{x}, t) / \partial t = D_v \nabla^2 v + (u - v) \times \beta, \quad (\text{S3b})$$

where D_u, D_v are the diffusion coefficients, α, β the reaction coefficients. In this work, we generate the simulation trajectory within $\Omega \in [0, 128]^2$ and $t \in [0, 6](s)$, using a 4th-order Runge–Kutta time integration method [61] under the periodic condition. Here, we define $D_u = 1, D_v = 100, \alpha = 0.01, \beta = 0.25, \Delta t = 0.002(s)$ and $\Delta x = 1$.

Gray-Scott Equation. As a coupled reaction-diffusion PDE, Gray-Scott equation consists of a velocity $\mathbf{u} = [u, v]^T$. For example, given a 3D field, the corresponding form of each component on $\mathbf{x} = (x, y, z) \in \mathbb{R}^3$ and $t \in [0, T]$ is as follows:

$$\partial u(\mathbf{x}, t) / \partial t = D_u \nabla^2 u - uv^2 + \alpha(1 - u), \quad (\text{S4a})$$

$$\partial v(\mathbf{x}, t) / \partial t = D_v \nabla^2 v + uv^2 - (\beta + \alpha)v, \quad (\text{S4b})$$

where D_u and D_v are the variable diffusion coefficients, β the conversion rate, α the in-flow rate of $u(\mathbf{x}, t)$ from the outside, and $(\alpha + \beta)$ the removal rate of $v(\mathbf{x}, t)$ from the reaction field. In this work, we generate the 2D simulation trajectory within $\Omega \in [0, 96]^2$ and the 3D simulation trajectory within $\Omega \in [0, 48]^3$ in $t \in [0, 750](s)$, using a 4th-order Runge–Kutta time integration method [61] under the periodic condition. Here, we define $D_u = 0.2, D_v = 0.1, \alpha = 0.025, \beta = 0.055, \Delta t = 0.25(s)$ and $\Delta x = 2$.

Black Sea Dataset. The BS dataset¹ provides measured data of daily mean sea surface temperature T and water flow velocities \mathbf{u} on the Black Sea over several years. The collection of these data was completed by Euro-Mediterranean Center on Climate Change (CMCC) in Italy starting from June 1, 1993, to June 30, 2021, with a horizontal resolution of $1/27^\circ \times 1/36^\circ$.

Note that the first three systems were spatiotemporally down-sampled (e.g., 5-fold in time) from high-fidelity data, while the last one was collected from field measurements.

D.2 Supplementary details of baseline

Graph Attention Network (GAT). GAT [70] proposed a graph network with a masked self-attention mechanism, aiming to address the shortcomings of graph convolutions.

Graph Attention Network Variant (GATv2). GATv2 [9] proposed a dynamic graph attention variant to remove the limitation of static attention in complex controlled problems, which is strictly more expressive than GAT.

¹https://data.marine.copernicus.eu/product/BLKSEA_MULTIIYEAR_PHY_007_004/description

Table S2: Summary Information of Datasets. Note that the trajectory number for training, validation, and testing is described by the form like (5/2/3).

Dataset	Space Interval	Time Interval	PDE Formulation	Boundary Condition	Number of Trajectories	Number of Nodes	Trajectory Length	Force Term
2D Burgers	$\Delta x = 0.02$	$\Delta t = 0.001$ s	Eq. S2	Periodic	40 (30/5/5)	2,500 (50^2)	1000	No
2D FN	$\Delta x = 1$	$\Delta t = 0.002$ s	Eq. S3	Periodic	10 (5/2/3)	16,384 (128^2)	3000	No
2D GS RD	$\Delta x = 2$	$\Delta t = 0.25$ s	Eq. S4	Periodic	10 (5/2/3)	2304 (48^2)	3000	No
3D GS RD	$\Delta x = 2$	$\Delta t = 0.25$ s	Eq. S4	Periodic	6 (2/2/2)	13,824 (24^3)	3000	No
2D BS	N/A	$\Delta t = 1$ day	–	N/A	24 (20/2/2)	1,000-20,000	365	N/A

Table S3: Summary analysis of Baselines.

Model	Grid Domain	Irregular Domain	Basis function Construction	Spectrum Network	Graph Network	Attention Network	Multiscale Modeling	Geometric Learning	High-order Modeling
GAT	✓	✓	✗	✗	✓	✓	✗	✗	✗
GATv2	✓	✓	✗	✗	✓	✓	✗	✗	✗
MGN	✓	✓	✗	✗	✓	✗	✗	✓	✗
MP-PDE	✓	✓	✗	✗	✓	✗	✗	✓	✗
FNO	✓	✗	✗	✓	✗	✗	✗	✗	✗
FFNO	✓	✗	✓	✓	✗	✗	✗	✗	✗
Geo-FNO	✓	✓	✗	✓	✗	✗	✗	✗	✗
Transolver	✓	✓	✗	✗	✗	✓	✓	✓	✗
Ours	✓	✓	✓	✗	✓	✗	✗	✓	✓

MeshGraphNet (MGN). MGN [56] provided a type of neural network architecture designed specifically for modeling physical systems that can be represented as meshes or graphs. Specifically, its “Encoder-Processor-Decoder” architecture in [56] has been widely adopted in many supervised learning tasks, such as fluid and solid mechanics constrained by PDEs. Relevant parameters are referenced from [56].

MP-Neural-PDE Solver (MP-PDE). MP-PDE [8] proposed the temporal bundling and push-forward techniques to encourage zero-stability in training autoregressive models. Relevant parameters are referenced from [8].

Fourier Neural Operator (FNO). The most promising spectral approach, FNO [42] proposed a neural operator in the Fourier domain to model dynamics. In this work, it was implemented for 2D and 3D spatial grid domains. The hyperparameters are taken from [42].

Factorized Fourier Neural Operator (FFNO). Factorized Fourier Neural Operator (FFNO) [68] factorizes the representation into separable Fourier representation to reduce the spatial and temporal complexity, improving its scalability. Relevant parameters are referenced from [68].

Geometry-informed FNO (Geo-FNO). Geometry-informed FNO (Geo-FNO) [39, 41] maps the irregular domain into a uniform grid,

preserving the computation efficiency and handling the arbitrary geometries. Relevant parameters are referenced from [39].

Transolver. Transolver [74] proposed a new Physics Attention to adaptively split the discretized domain into a series of learnable slices of flexible shapes, effectively capture intricate physical correlations under complex geometrics. Relevant parameters are referenced from [74].

D.3 Supplementary details of results

D.3.1 Summary of parameters of all models.

Overall settings. As shown in Table S4, the default number of layers is 4; the learning rate is 1×10^{-4} ; the hidden dimension is 128; the batch size is 100; the standard deviation of training noise is 1×10^{-4} . We offer the basic parameter sets of each baselines in the prediction tasks.

In addition, we list the different parameters of all models on various datasets in Tables S5 to S13, such as the mode size in FNO and the number of head in the attention mechanism.

D.3.2 Data scaling test. We also have performed a data scaling test and report the results (data size vs. prediction error) in the Table S14 below to support our claim of low data requirement.

D.3.3 Discussion of the position information in cells. In this part, we provide other two cases “CeFeGNN w/o Cell Pos.” and “w Pos. to B” in the following Table S15, where “w/o Cell Pos.” represents

Table S4: Default Training settings for all models. Note that the model’s performance does not monotonically improve with increasing parameters. Note that we offer the parameter sets that achieved relative peak performance for each baselines in the prediction tasks.

Model	GAT	GATv2	MGN	MP-PDE	FNO	FFNO	Geo-FNO	Transolver	Ours
No. of Layers	4	4	4	4	4	4	4	4	4
Std. of Noise	0.0001	0.0001	0.0001	0.0001	0.0001	0.0001	0.0001	0.0001	0.0001
Learning rate	0.0001	0.0001	0.0001	0.0001	0.0001	0.0001	0.0001	0.0001	0.0001
Hidden dimension	128	128	128	128	128	128	128	128	128
Batch size	100	100	100	100	100	100	100	100	100
No. of Parameters	779,014	778,630	514,236	528,658	541,436	1,072,388	1,482,674	1,516,354	1,482,674

Table S5: Different training hyperparameters for GAT. The default attention head is 1.

Dataset	Attention head	Batch size	No. of Parameters
3D GS RD	1	5	779,014
2D BS	1	20	805,350

Table S6: Different training hyperparameters for GATv2. The default attention head is 1.

Dataset	Attention head	Batch size	No. of Parameters
3D GS RD	1	5	778,630
2D BS	1	20	804,966

Table S7: Different training hyperparameters for MGN.

Dataset	Batch size	No. of Parameters
3D GS RD	5	514,236
2D BS	20	540,572

Table S8: Different training hyperparameters for MP-PDE. The default training length is 2.

Dataset	Training length	Batch size	No. of Parameters
3D GS RD	2	5	528,658
2D BS	2	20	554,994

Table S9: Different training hyperparameters for FNO. The default mode size is 8.

Dataset	No. of mode	Batch size	No. of Parameters
3D GS RD	8	10	4,515,746

Table S10: Different training hyperparameters for FFNO. The default mode size is 8.

Dataset	No. of mode	Batch size	No. of Parameters
3D GS RD	8	10	1,334,660

Table S11: Different training hyperparameters for Geo-FNO. The default mode size is 8 and the mapping size is 32×32 .

Dataset	No. of mode	Mapping size	Batch size	No. of Parameters
3D GS RD	8	$32 \times 32 \times 32$	10	2,705,569
2D BS	8	32×32	20	727,557

Table S12: Different training hyperparameters for Transolver. The default attention head is 8 and the mapping size is 8×8 .

Dataset	Attention head	Mapping size	Batch size	No. of Parameters
3D GS RD	8	$8 \times 8 \times 8$	10	1,631,042
2D BS	8	8×8	20	1,516,739

Table S13: Different training hyperparameters for CeFeGNN. The default window size is 4.

Dataset	Window size	Batch size	No. of Parameters
3D GS RD	4	5	1,482,674
2D BS	4	20	1,509,010

Table S14: Data scaling test under RMSE metric of CeFeGNN, MGN and MP-PDE on 2D Burgers equation.

Model	No. of layers	Dimension	Data size		
			30	40	50
CeFeGNN	4	128	0.00664	0.00413	0.00226
MGN	4	128	<u>0.01174</u>	<u>0.00926</u>	<u>0.00636</u>
MP-PDE	4	128	0.01784	0.01442	0.00911

the cell initial feature without the position awareness, and “w Pos. to B” is replacing the distance to the cell center with the distance to the nearest PDE boundary. The results in Table S15 show that the performance improvement of CeFeGNN is not only due to add position awareness into the cell initial feature, but also the second-order refinement of the discrete space.

Table S15: Quantitative ablation results about the cell position information for CeFeGNN and other two cases under RMSE metrics.

Model	RMSE ↓				
	Burgers (0.001s)	FN (0.002s)	2D GS (0.25s)	3D GS (0.25s)	BS (1day)
CeFeGNN	0.00664	0.00364	0.00248	0.00138	0.55599
w/o C Pos.	0.00721	0.00477	0.00439	0.00274	0.56098
w Pos. to B	0.00720	0.00490	0.00445	0.00276	0.56040
MGN	0.01174	0.02108	0.02917	0.01925	0.61475

D.3.4 Discussion with other Higher-order Graphs. In this part, we mainly focus on discussing the excellent works CCNNs in [26] and MPSNs in [7]. A summary of these models is shown in the following Table S16.

Table S16: Summary of CeFeGNN, MGN, CCNNs, and MPSNs

Model	Message Level	Complex Predefinition	Complex Type	Application
CeFeGNN	2	No	3	Dynamics
MGN	2	No	2	Dynamics
CCNNs	3	No	3	Classification
MPSNs	2	Yes	5	Classification

Firstly, MGN achieves message passing through a two-level structure (*edge* → *node*). On this basis, CCNNs in [26] leverages combinatorial complexes to achieve message passing through a three-level structure (*cell* → *edge* → *node*). Meanwhile, MPSNs in [7] performs message passing through a two-level structure (*complexes* → *simplex*) on various simplicial complexes (SCs), which primarily include one simplex (node) and four types of complexes with varying adjacent simplices (e.g., boundary adjacencies, co-boundary adjacencies, lower-adjacencies, and upper-adjacencies), to enhance feature distinguishability and thus improve classification performance.

In contrast, CeFeGNN sets apart from these works and adopts a novel two-level structure (*[cell, edge]* → *node*) from the spatial perspective, which is more suitable to learn implicit dynamic mechanism.

Since there are only node labels for the supervised learning, the three-level message passing mechanism in [26] poses significant training challenges. However, our two-level message passing sequence reduces the high coupling degree in [26] and avoids the limitation for additional predefined special complexes (e.g., some simplicial complexes in [7]). A comparison result between two-level and three-level mechanisms is shown in the following Table S17. The results in Table S17 demonstrate that three-level mechanism underperforms than two-level mechanism in our all cases.

Table S17: Comparison result between two-level and three-level mechanisms with various time intervals (Δt).

Model	RMSE ↓				
	Burgers (0.001s)	FN (0.002s)	2D GS (0.25s)	3D GS (0.25s)	BS (1day)
CeFeGNN	0.00664	0.00364	0.00248	0.00138	0.55599
MGN (2-level)	0.01174	0.02108	0.02917	0.01925	0.61475
MGN (3-level)	0.03220	0.04196	0.05884	0.08218	0.61524

Table S18: Statistic information of traffic datasets (PeMS03 and PeMS04). Here, “F” represents the traffic flow, “S” the traffic speed, and “O” the traffic occupancy rate.

Property	PeMS03	PeMS04
No. of nodes	358	307
No. of time steps	26,208	16,992
Sampling time	5 min	5 min
Time range (in 2018)	09.01–11.30	01.01–02.28
Variable	F	F, S, O
Training/Validation/Test	0.6/0.2/0.2	0.6/0.2/0.2

Table S19: Ablation Results on PeMS03 and PeMS04 with the MAE, RMSE, and MAPE (%) metric. The abbreviation “C” represents the cell.

Model	PeMS03 ↓			PeMS04 ↓		
	MAE	RMSE	MAPE	MAE	RMSE	MAPE
CeFeGNN	14.08	24.14	14.45	17.91	29.28	11.86
w/o C	14.87	25.66	14.95	18.21	29.82	11.98
w/o FE	14.92	25.42	14.99	18.29	29.91	11.99
w/o C, FE	15.31	27.33	15.14	18.40	30.26	12.13

D.3.5 Extension on traffic prediction. For providing a more comprehensive evaluation, we conduct experiments on traffic forecasting tasks, where stronger empirical evidence could better substantiate the model’s effectiveness. As shown in Table S20, we provide the results on traffic datasets (PeMS03 and PeMS04, ² see Table S18 for more details.) and consider more related baselines, including StGCN [75], ASTGCN [77], AGCRN [5], STSGCN [65], STFGNN [38], ASTGNN [79], PDFormer [32], STAEformer [47], HTVGNN [15], FasterSTS [14], and DTRformer [13]. We can see that our model achieved overall the best performance.

In addition, a ablation study on PeMS03 and PeMS04 is provided in Table S19 to show the contributions of each components in our model. These results demonstrate the effectiveness of CeFeGNN.

D.3.6 Physical loss of PDE systems. In this work, our research objective is to learn a general model that can be applied in various scenarios, such as real-world prediction tasks (ocean data prediction and traffic prediction). Therefore, we **did not** incorporate hard physical constraints in the **training** process.

²<https://pems.dot.ca.gov/>

To evaluate the physical consistency of the model prediction on PDE systems, we added an analysis of the PDE loss during **inference (not training)** of our model, with the results summarized in Table S21. This allows us to quantitatively assess our model’s adherence to underlying physical principles without compromising its data-driven nature. It can be seen from Table S21 that our model achieved distinctively higher physical consistency compared with other suboptimal models (MGN, MP-PDE) in the paper.

Remark D.1. Our work learns spatiotemporal mappings directly from data (**data-driven**) applicable to generic systems **without prior knowledge** (e.g., a strong explicit prior knowledge in **equation-driven PINNs**) because PINNs fail to handle the complicated real-world BS example since **no convincing governing equations are available**.

Table S20: Results on PeMS03 and PeMS04 with the MAE, RMSE, and MAPE (%) metric.

Model	PeMS03 ↓			PeMS04 ↓		
	MAE	RMSE	MAPE	MAE	RMSE	MAPE
Transformer	17.50	30.24	16.80	23.83	37.19	15.57
STGCN	17.49	30.12	17.15	22.70	35.55	14.59
ASTGCN	17.69	29.66	19.40	22.93	35.22	16.56
AGCRN	16.06	28.49	15.85	19.83	32.26	12.97
STSGCN	17.48	29.21	16.78	21.19	33.65	13.90
STFGNN	16.77	28.34	16.30	19.83	31.88	13.02
ASTGNN	15.07	26.88	15.80	19.26	31.16	12.65
MGN	15.31	27.33	15.14	18.40	30.26	12.13
PDFormer	14.94	25.39	15.82	18.32	29.97	12.10
STAEformer	15.35	27.55	15.18	18.22	30.18	11.98
HTVGNN	<u>14.20</u>	24.26	<u>14.52</u>	<u>17.99</u>	<u>29.74</u>	<u>11.90</u>
FasterSTS	14.58	24.12	14.93	18.49	29.92	12.21
DTRformer	14.50	25.45	14.94	18.00	29.58	12.30
CeFeGNN	14.08	<u>24.14</u>	14.45	17.91	29.28	11.86

Table S21: Results of physical loss (aka, PDE residual loss).

Model	2D Burgers ↓	2D FN ↓	2D GS ↓
CeFeGNN	6.412×10^{-5}	6.994×10^{-5}	2.854×10^{-5}
MGN	12.01×10^{-5}	38.39×10^{-5}	45.11×10^{-5}
MP-PDE	18.96×10^{-5}	67.05×10^{-5}	87.53×10^{-5}

D.3.7 Effect of several temporal models on CeFeGNN. In our work, we employed **residual connections to model temporal marching** (see Eq. 4). Our model architecture can be summarized as "encoder → processor → decoder". Here we insert the TAN or LSTM before "decoder" (i.e., encoder → processor → TAN/LSTM → decoder). Following P0, we firstly set the training input step as 1 (same as the setting of CeGNN) with the results in Table S22.

Obviously, the reason for the TAN and LSTM failing in the case of 1 input step is that they do not learn the temporal dependencies as expected, but disrupt the spatiotemporal information transmission of the basic model.

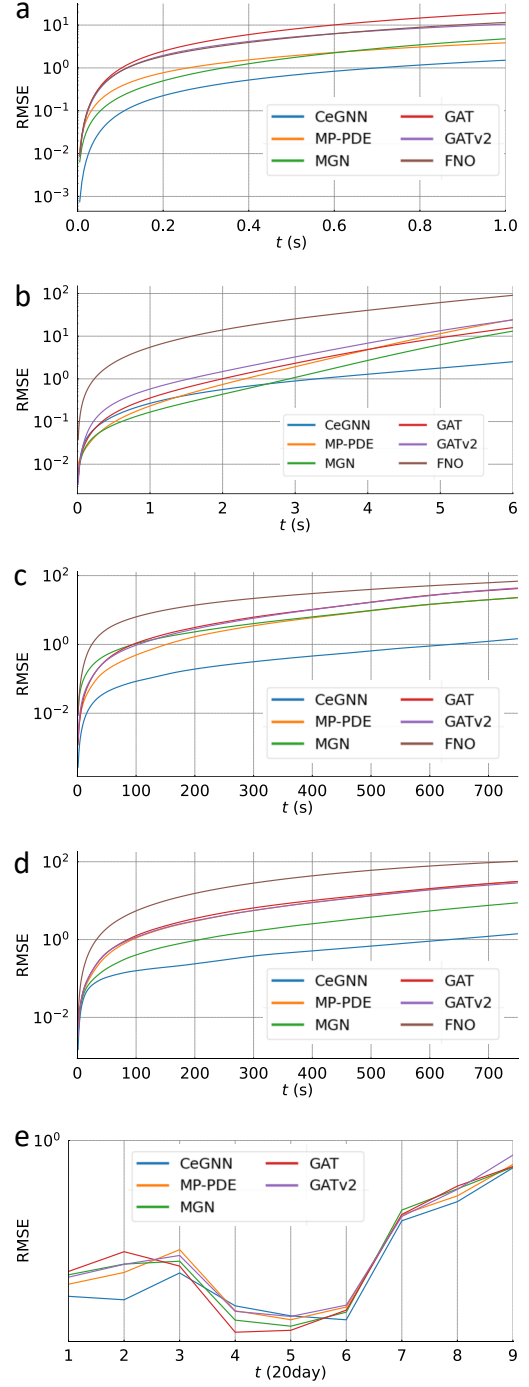


Figure S2: Error propagation curve on various systems. a, 2D Burgers equation. b, 2D FN equation. c, 2D GS equation. d, 3D GS equation. e, 2D BS dataset.

Therefore, we further conducted experiments with the setting of "N → N" (aka, next token generation; herein, we took N = 3 for illustration purpose) and summarized the results in Table S22. We can see that the temporal methods (TAN, LSTM) yield a performance

improvement in such a setting (however, still inferior to our model). This might be because such temporal modules add extra model complexity, which might bring over-fitting issues especially when the training data is limited. Note that the attention mechanism and the LSTM module bring a $2 \times$ increase of training speed.

Table S22: Results of varying training input length (k) on 2D Burgers equation.

Input step	k=1		k=3
	RMSE ↓	RMSE ↓	Training time (s/epoch)
CeFeGNN	0.0066	0.0049	17.31
CeFeGNN + TAN	<u>0.0981</u>	<u>0.0584</u>	<u>38.13</u>
CeFeGNN + LSTM	0.1293	0.0689	39.86

D.3.8 Error propagation curve. In this part, we provide the error propagation curves of CeFeGNN and several representative models on all benchmarks, as shown in Figure S2.

D.3.9 Full snapshots. In this part, we provide the full snapshots of CeFeGNN and several representative models on 3D GS and 2D BS benchmarks, as shown in Figures S3 and S4.

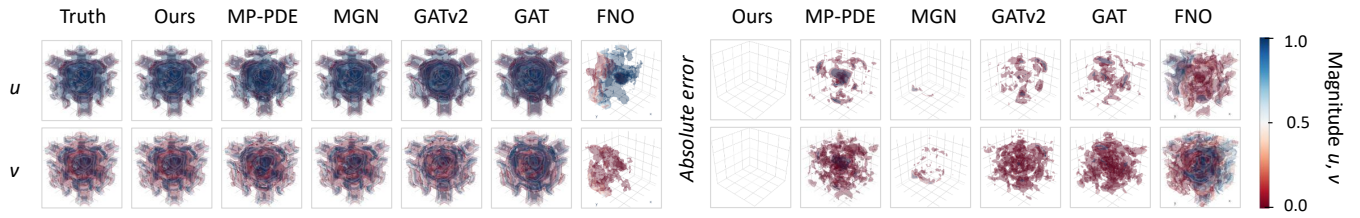


Figure S3: Full snapshots on 3D GS equation. The absolute error represents the absolute difference between ground-truth data and the prediction values.

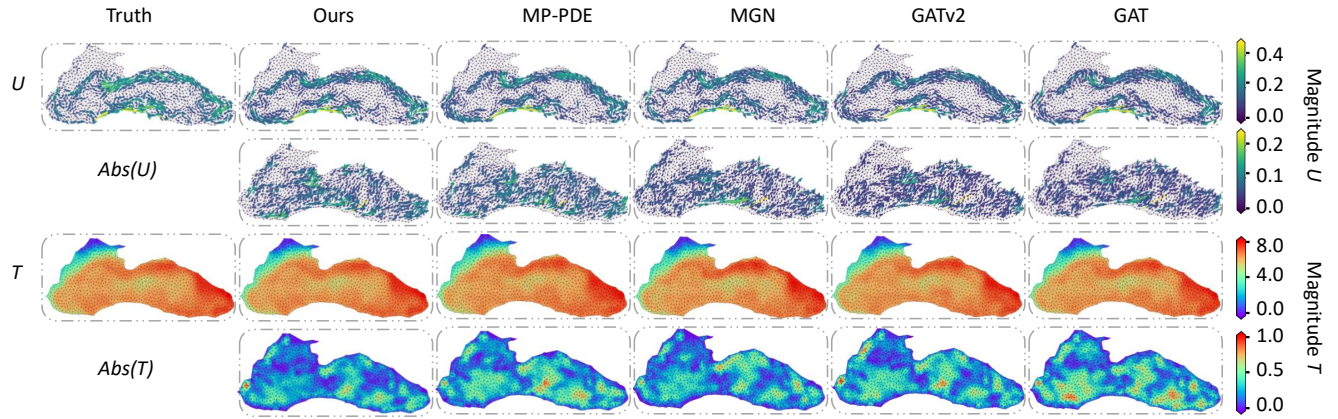


Figure S4: Full snapshots on 2D BS dataset. The “Abs(-)” represents the absolute difference between ground-truth data and the prediction values